Chapter 1 General Introduction

1. 1 Superconductivity – The basic phenomena

The electrical resistance of many metals and alloys vanishes abruptly when they are cooled below a certain temperature, which is a characteristic of the material. This phenomenon of superconductivity was discovered by Kamerlingh Onnes [1] in Leiden in 1911, three years after he first liquefied helium. At the critical temperature T_c, the material undergoes a phase transition from a state of normal electrical resistivity to a superconducting state with no resistivity as schematically shown in Fig. 1.1. Thus, perfect conductivity is the first important property of superconductivity.

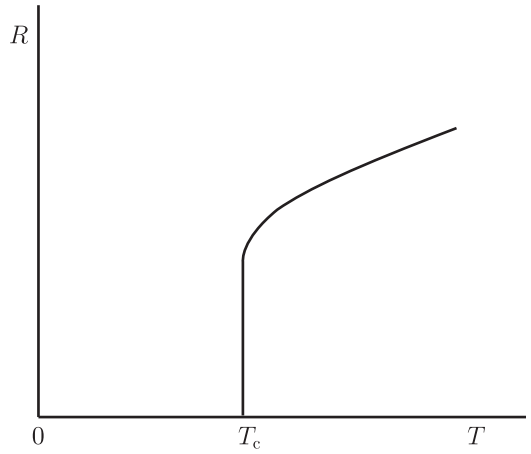

Fig. 1.1: Variation in electrical resistance versus temperature.

Another important property of superconductivity is perfect diamagnetism. In 1933 two German physicists, Meissner and Ochenfeld [2], found that superconductors expel magnetic field: if a superconductor in its normal state is put in a magnetic field, and the temperature is lowered below the critical temperature (where the material becomes superconductive) the magnetic field is expelled . When a magnetic field is applied to a superconducting substance, the magnetic field can not penetrate the substance. These diamagnetic phenomena are called the Meissner effect, as shown in Fig. 1.2. From its feature of zero resistivity, the superconductor may be regarded as a perfect conductor. However, zero resisitivity is not the essential feature of superconductivity but rather a result of a more essential feature, diamagnetism.

Another essential property of superconductors is Josephson effect, which was first

predicted by Josephson in 1962 [3] and later confirmed by Anderson and Rowell in 1963 [4]. Superconducting electrons can tunnel through a thin insulator sandwiched by two superconducting layers. Such a device is called Josephson junction (see Fig. 1.3).

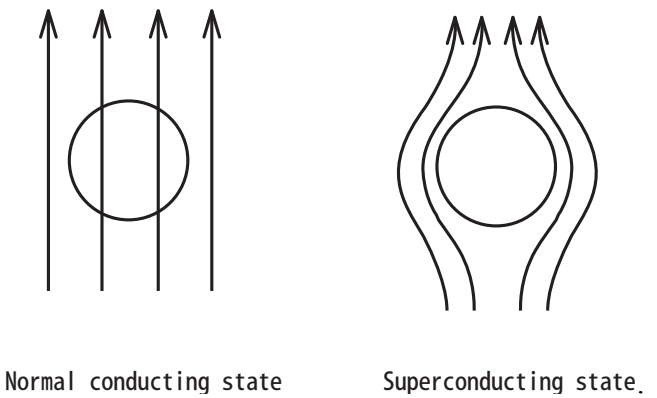

Fig. 1.2: Meissner effect

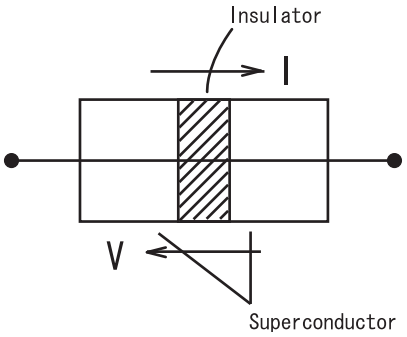

Fig. 1.3: Josephson junction

1. 2 Type-1 and Type-2 superconductors

There are two kinds of superconductor, type-1 and type-2. These are classified with respect to their magnetic properties.

The magnetization of a type-1 superconductor is shown in Fig. 1.4(a). When the external magnetic field H_e is lower than some critical field H_c, the magnetization M is given by

$$M = -H_e \qquad (1.1)$$

and the superconductor shows a perfect diamagnetism ($B = 0$). It is in the Meissner state. The transition from the superconducting state to the normal state occurs at the $H_e = H_c$ with a discontinuous variation of the magnetization to $M = 0$ (i.e. $B = \mu_0 H_e$ with μ_0 denoting the permeability of vacuum).

For a type-2 superconductor, on the other hand, the perfect diamagnetism given by Eq. (1.1) is maintained only up to the lower critical field, H_{c1}, and then the magnetization varies continuously with the penetration of magnetic flux as shown in Fig. 1.4(b) until the magnetic field reaches the upper critical field, H_{c2}, where the normal state starts. The partially diamagnetic state between H_{c1} and H_{c2} is called the mixed state.

It is empirically known that the critical field of type-1 superconductors varies with

temperature according to

$$H_{\mathrm{c}}(T) = H_{\mathrm{c}}(0)\left[1-\left(\frac{T}{T_{\mathrm{c}}}\right)^2\right], \qquad (1.2)$$

where $H_{\mathrm{c}}(0)$ is the critical field at zero temperature. The lower and upper critical fields of type-2 superconductors show similar temperature dependences. Obviously they reduce to zero at the critical temperature T_{c}. The phase diagrams of type-1 and type-2 superconductors on the temperature-magnetic field plane are shown in Fig. 1.5(a) and 1.5(b), respectively.

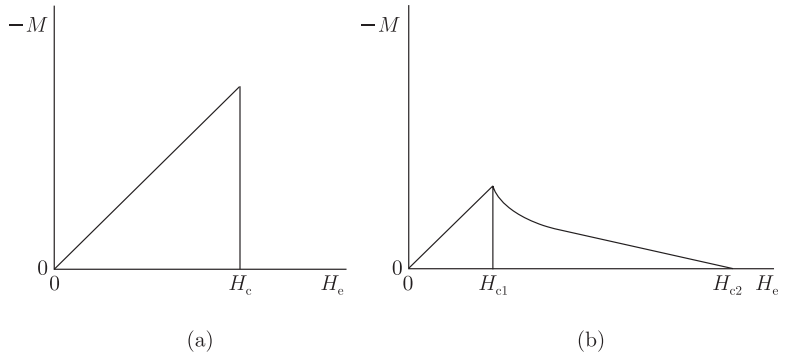

Fig. 1.4: Magnetic field dependence of magnetization for (a) type-1 superconductor and (b) type-2 superconductor.

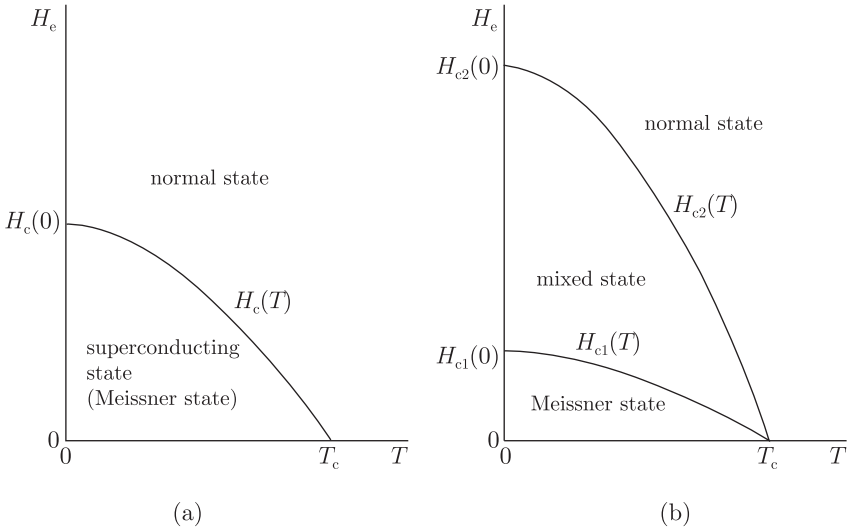

Fig. 1.5: Phase diagram on the magnetic field vs temperature plane for (a) type-1 superconductor and (b) type-2 superconductor.

1. 3 Superconducting materials

A number of superconducting materials have emerged after the discovery of superconductivity of mercury in 1911. Several pure metals (e.g., Pb, Nd, Al), alloys (e.g., PbBi, NdTi), and intermetallic compounds (e.g., Nd_3Sn, Nb_3Ga, Nb_3Ge) are known to show superconductivity along with oxides, nitrides and organic materials. These superconductors are called low temperature superconductors. Until 1986, the highest critical temperature remained 23 K of Nb_3Ge, which had been discovered in 1971. In 1980s, many physicists believed that superconductivity at temperature above 25 K was impossible so long as the superconductivity mechanism is based on the electron-phonon interaction.

The discovery of La-Ba-Cu-O by Bednorz and Muller [5], which exhibits T_c = 30 K, opened the way to the synthesis of various novel higher T_c superconductors. In 1987 Wu *et al*. [6] discovered $YBa_2Cu_3O_7$, which is the first superconductor with T_c above the boiling point of nitrogen (T_c = 90 K), followed by the discovery of other important members of the oxide superconductors, such as the Bi-Sr-Ca-Cu-O [7] and Tl-Ba-Ca-Cu-O [8], and Hg-Ba-Ca-Cu-O [9] compounds. Today, the highest record T_c is 145 K marked by Hg-Ba-Ca-Cu-O under high pressure of several tens of GPa [10]. It is interesting that all oxide superconductors consists of superconducting CuO_2 sheets separated by non–superconducting block layers. These oxide superconductors are called high temperature superconductors (HTS).

1. 4 Applications of superconductivity

Superconductivity was discovered in a physics laboratory and it is perhaps not surprising that it should have been used there. Starting with small-scale laboratory experiments and then moving into the big science of high energy physics, superconducting magnets have become widely accepted as an essential research tool. There are various potential applications of superconductors as listed in Table 1.1.

Table1.1: The applications of superconductors.

Applications	Purpose
Superconducting filters	Electronics
Superconducting Quantum Interference Devices (SQUID)	Sensor

Power cables, fault current limiter, HTS transformer, generators, superconducting energy storage system (SMES), magnetic bearing for superconducting flywheel energy storage	Power applications
High field magnet for magnetic resonance imaging (MRI)	Medical science
Powerful magnet for magnetic levitated train	Magnetic levitation
High field magnet for single crystal pulling, steel manufacturing, magnetic separation current leads, bulk magnet, magnetic bearing	Industrial processing
High field magnet for accelerators, NMR	Research

1. 5 Flux pinning

The critical current density, J_c, the maximum steady current density that a superconductor can carry without an electric resistance, is one of the most important parameters of the superconductor for its applications. This characteristic property is determined by flux pinning interactions by defects called pinning centers such as normal precipitates, grain boundaries, dislocations, stacking faults, etc. That is, the Lorentz force works on quantized flux lines in the superconductor when the transport current is applied, and the pinning centers prevent flux lines from moving, resulting in no appearance of the electric field. The corresponding force density caused by the pinning centers is called the pinning force density, F_p. The relationship between J_c and F_p is $J_c = F_p/B$. Hence, it is desired to enhance the pinning force to improve the J_c properties in superconductors. In this subsections the Ginzburg-Landau (G-L) theory, the free energy of superconductors and the general features of elementary flux pinning are described.

1. 5. 1 G-L theory and free energy of a superconductor

The Ginzburg and Landau (GL) theory [11] describes superconductivity in terms of the

order parameter, Ψ, as a complex number and the square of its magnitude $|\Psi|^2$ gives the number density of superconducting electrons. The free energy of a superconductor depends on this density of superconducting electrons, and hence, is a function of $|\Psi|^2$. In the vicinity of the transition point $|\Psi|^2$ is expected to be sufficiently small that the free energy can be expanded as a power series of $|\Psi|^2$:

$$\text{Const.} + \alpha|\Psi|^2 + \frac{\beta}{2}|\Psi|^4 + \quad \ldots, \tag{1.3}$$

where α and β are the coefficients. For the purpose of describing the phase transition between the superconducting and normal states, the expansion up to the $|\Psi|^4$ terms is sufficient.

It is speculated that the order parameter varies spatially due to the existence of the magnetic field. By analogy with quantum mechanics, this should lead to a kinetic energy. The expected value of the kinetic energy is written in terms of the momentum operator known in the quantum mechanics as

$$\frac{1}{2m^*}\Psi^*(-i\eta\nabla + 2e\vec{A})^2\Psi, \tag{1.4}$$

where Ψ^* is the complex conjugate of Ψ and m^* is the mass of the superconducting electron, the Cooper pair, and we used the fact that the electric charge of the Cooper pair is -2*e*. The operator of the momentum takes the well known form containing the vector potential, $\vec{A}$, so that the Lorentz force on a moving charge is automatically derived. From the Hermitian property of the operator the kinetic energy in Eq. (1.4) is written as

$$\frac{1}{2m^*}\left|\left(-i\eta\nabla + 2e\vec{A}\right)\Psi\right|^2. \tag{1.5}$$

Thus, the free energy density in the superconducting state including the energy of magnetic field is given by

$$F_s = F_n(0) + \alpha|\Psi|^2 + \frac{\beta}{2}|\Psi|^4 + \frac{1}{2\mu_0}(\nabla\times\vec{A})^2 + \frac{1}{2m^*}\left|(-i\eta\nabla + 2e\vec{A})\Psi\right|^2. \tag{1.6}$$

The second and third terms are the condensation energy density, the fourth term is magnetic field energy density and the fifth term is the kinetic energy density.

When the superconductor coexists with the magnetic field, $\Psi(\vec{r})$ and $\vec{A}(\vec{r})$ are

determined so that the free energy, $\int F_s \mathrm{d}V$, is minimized. Hence, the variation of $\int F_s \mathrm{d}V$ with respect to $\Psi^*(\vec{r})$ and $\vec{A}(\vec{r})$ are required to be zero and the following two equations are derived:

$$\frac{1}{2m^*}(-i\eta\nabla + 2e\vec{A})^2\Psi + \alpha\Psi + \beta|\Psi|^2\Psi = 0, \tag{1.7}$$

$$\vec{j} = \frac{i\eta e}{m^*}(\Psi^*\nabla\Psi - \Psi\nabla\Psi^*) - \frac{4e^2}{m^*}|\Psi|^2\vec{A}, \tag{1.8}$$

with

$$\vec{j} = \frac{1}{\mu_0}\nabla\times\nabla\times\vec{A}. \tag{1.9}$$

The above two Eqs. (1.7) and (1.8) are called the Ginzberg-Landau or the G-L equations.

The electromagnetic properties in the superconductor are determined by two characteristic lengths, i.e. λ, the penetration depth of magnetic field and ξ, the coherence length. These are related to the spatial variations of the magnetic flux density *B* and the order parameter Ψ. In terms of G-L theory λ and ξ are expressed as

$$\lambda = \left(\frac{m^*}{4\mu_0 e^2|\Psi_\infty|^2}\right)^{1/2}, \tag{1.10}$$

$$\xi = \frac{\eta}{(2m^*|\alpha|)^{1/2}}, \tag{1.11}$$

where Ψ_∞ denoting the equilibrium value of Ψ in the absence of magnetic field. $|\Psi|^2$ is almost zero being close to normal state in the region of distance of about the coherence length, ξ from the center of flux lines as shown in Fig. 1.6. Hence this region is called a normal core.

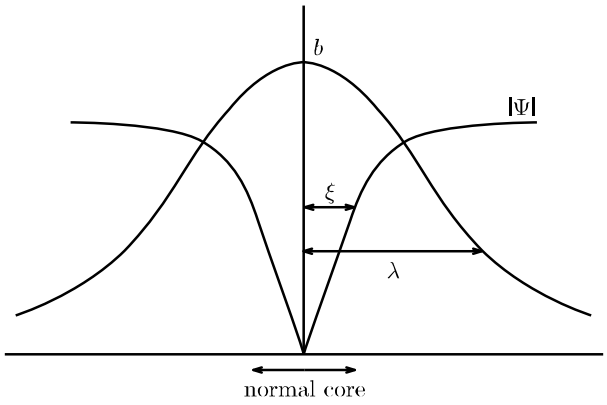

Fig. 1.6: Spatial variations of the order parameter $|\Psi|^2$ and B the magnetic flux density in an isolated flux line.

1. 5. 2 The general features of elementary flux pinning

The flux pinning interaction occurs when flux lines in a superconductor meet defects or regions with other chemical compositions which are called pinning centers. The flux line has structures of the magnetic field density, B, and the order parameter, Ψ, as shown in Fig. 1.6. Hence, when flux line passes through a defect at which material parameters are different from the matrix superconductor, the energy of flux line changes, resulting in a flux pinning interaction. The maximum force of the interaction that one pinning center can exert on a flux is called the elementary pinning force. The magnitude of the pinning force density depends entirely on the strength of pinning centers and their concentration. The free energy around an inhomogeneity can be expressed by Eq. (1.4) in terms of Ginzberg-Landau theory. In this case, the coefficients α and β vary spatially around the inhomogeneity. The superconducting order parameter Ψ and the magnetic flux density $\vec{B} = \mathrm{rot}\vec{A}$ also vary around the normal core of a flux, as shown Fig. 1.6. When the flux meets inhomogeneity, Ψ and $\vec{A}$ are deformed. Hence, the free energy $U = \int F_s \mathrm{d}V$ integrated around the inhomogeneity varies according to the virtual displacement x of the flux. Thus, the elementary pinning force of the inhomogeneity is defined by

$$f_p = \left(-\frac{\partial U}{\partial x} \right)_{\max}.$$

Fig. 1.7(a) schematically shows the variation of energy U during a displacement of flux line across a pinning center, and Fig. 1.7(b) shows the corresponding interaction force.

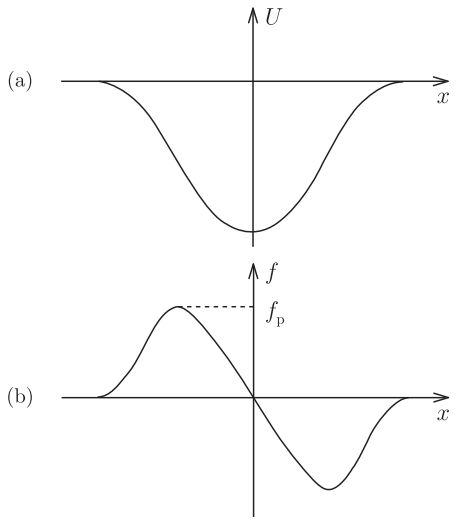

Fig. 1.7: (a) Variation of energy when a flux line passes through a pinning center and (b) the variation of the pinning force.

1. 6 The feature of RE-123 superconductors

During last few years technology of RE-123 superconductors has experienced a vivid development that puts these compounds on a top position among materials for 21^{1st} century. Y-123 was the first compound discovered by Wu *et al*. [6] in 1987 having a T_c above the temperature of liquid nitrogen. Soon after the discovery of Y-123, RE-$Ba_2Cu_3O_{7-\delta}$ are found to be superconducting for RE(rare earth) = La, Nd, Sm, Eu, Gd, Dy, Ho, Er, Tm, Yb, Lu [24]. They offer a broad scale of engineering applications like superconducting permanent magnets, magnetic bearings, superconducting electric motors, magnetic separating devices for water purification, current leads, non-contact transport systems, flywheel energy storage systems, etc., [12-18], some of them being, according to the latest reviews [19-23], ready for introduction to the market in a close future. Now, RE-123 superconductors are well known oxide superconductors whose T_c's are above 90 K, shown in Table 1.2

Table1.2: RE-123 superconductors and their transition temperature [25]

Rare earth compounds	T_c (K)
$YBa_2Cu_3O_{7-\delta}$	93.4
$NdBa_2Cu_3O_{7-\delta}$	95.3
$SmBa_2Cu_3O_{7-\delta}$	93.5

$EuBa_2Cu_3O_{7-\delta}$	94.9
$GdBa_2Cu_3O_{7-\delta}$	93.8
$DyBa_2Cu_3O_{7-\delta}$	92.7
$HoBa_2Cu_3O_{7-\delta}$	92.9
$ErBa_2Cu_3O_{7-\delta}$	92.4
$TmBa_2Cu_3O_{7-\delta}$	92.5
$YbBa_2Cu_3O_{7-\delta}$	87.0
$LuBa_2Cu_3O_{7-\delta}$	89.5

The RE-$Ba_2Cu_3O_{7-\delta}$ superconductors are a broad family of perovskites-type oxides with unique properties. Now, the family of RE-123 materials consists of all simple compounds and a rich variety of their combinations, binary, ternary or quarternary ones. It became a typical representative of high-T_c materials. RE-123 materials have been prepared and studied in the form of thin films, multilayers, single crystals, ceramics, melt-textured samples, and other forms. Nowadays the most promising for bulk applications are melt-textured Y-123 and ternary systems (Nd, Eu, Gd)-123, (Nd, Sm, Gd)-123 and (Sm, Eu, Gd)-123 prepared in reduced oxygen atmosphere.

1. 6. 1 Impact of melt-processing in RE-123 superconductors

Recent progress in the melt-processing of bulk high-temperature superconductors has created a basis for various engineering applications. For most power applications high critical current density J_c and irreversibility field B_i are substantial. The irreversibility field, B_i, is an important parameter representing a maximum applicable magnetic field for a practical use of superconductor at which critical current density, J_c, is reduced to zero and which is determined in terms of a criterion of the critical current density, J_c. With respect to an effective cooling, the most interesting temperature for applications is liquid nitrogen, 77.3 K. Therefore, high J_c and B_i at this rather high temperature are extremely desired.

At present, melt texturing is the most eminent technique used for the preparation of bulk high-temperature superconducting materials, since this process leads to superior transport and magnetic properties. This method was introduced by Jin *et al.* [26] for the Y-123 system, and denoting as a melt-texture-growth (MTG). To improve the quality of large oriented 123 grains, Salama *et al*., developed the liquid phase processing (LPP) [27]. In the following several years tremendous progress in melt-processing techniques has been made that brought a number of similar melt growing techniques, for example the melt-powder-melt-growth (MPMG) [28], the quench-melt-growth (QMG) [29], the

powder-melt-process (PMP) [30], the solid-liquid-melt-growth (SLMG) [31] and the melt-quenched-pressurized partial-melt-growth (MQPPMG) [32].

In the rare earth (RE) elements La, Nd and Sm, it has been unsuccessful to fabricate melt-processed RE-$Ba_2Cu_3O_{7-\delta}$ superconductors with high T_c (> 90 K) and sharp transition. The T_c of La-123, Nd-123 and Sm-123 are relatively low when they are melt processed in air. This is due to the fact that the RE-123 systems (RE; La, Nd, Sm, Eu, Gd) have RE-Ba solid solution; RE substitutes on the Ba site, and thus $RE_{1+x}Ba_{2-x}Cu_3O_{7-\delta}$ type solid solution is formed. Since the ionic radii of the RE elements approach that of Ba, it allows a large degree of substitution of the RE^{3+} for Ba without forming second phase. Thus, the equilibrium phase diagram changes with RE, in that RE-123 is no longer a point compound as shown in Fig. 1.8. The maximum amount of the substitution of the RE for Ba scales with the ionic radius as shown in Fig. 1.9. Superconductivity of p-type doped systems is dependent on the holes predominantly on the oxygen sites in the CuO_2 planes; therefore, the substitution of an RE with 3+ valences for a Ba with 2+ valences would require a donor electron in order to cancel a hole on the CuO_2 plane. The superconducting transition temperature should then decrease with increasing RE^{3+} substitution. Fig. 1.10 shows the superconducting transition temperature T_c of fully oxygenated $Nd_{1+x}Ba_{2-x}Cu_3O_{7-\delta}$ as a function of x. The orthorhombic to tetragonal phase transition for fully oxygenated samples occurs at around $x = 0.25$ and T_c decreases nonlinearly with x.

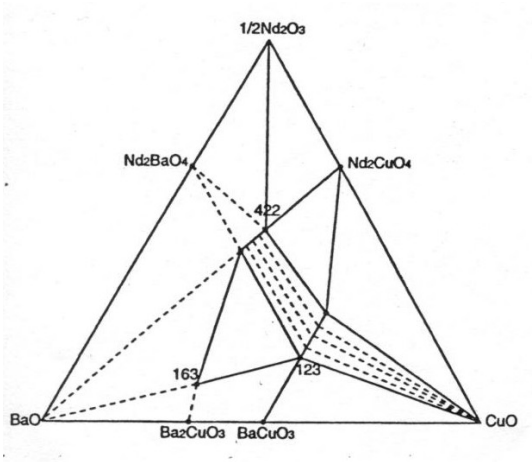

Fig. 1.8: Subsolidus phase diagram of the Nd-Ba-Cu-O system at 890^0C in air [33]. Note that Nd123 and Nd422 are not point compounds [Fig. 3 of ref. 34]

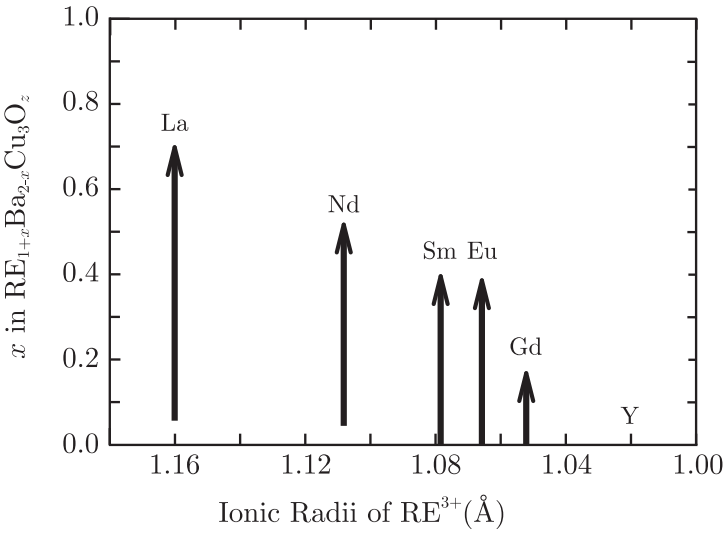

Fig. 1.9: The range of RE-Ba substitution for the RE123 system in air [Fig. 4 of ref. 34].

In 1993, Yoo *et al*. [35] found that RE-Ba substitution is suppressed when RE123 is melt-processed in a reduced oxygen atmosphere, which is termed the oxygen-controlled-melt-growth (OCMG) process. This process realized a sharp transition with keeping a higher superconducting transition temperature for RE123 than that of Y123. The PO_2 control during the melt growth was the most critical factor affecting T_c in all melt processing.

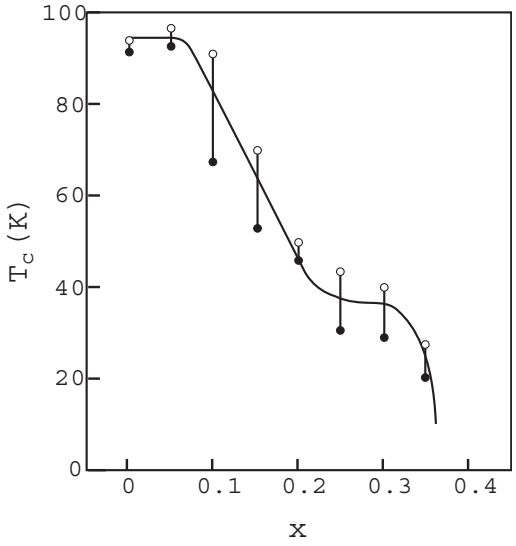

Fig. 1.10: T_c as a function of x for $Nd_{1+x}Ba_{2-x}Cu_3O_{7-\delta}$ samples, sintered at 1050^0C and

fully oxygenated, using an applied field of 5 mT. T_c corresponds to the 50 % of the field-cooled (FC) values at 10 K while the error bars indicate the 10 % and 90 % values [Fig. 5 of ref. [34]].

The effect of PO_2 during melt processing on the T_c is displayed in Fig. 1.11. It is obvious that a reduction of PO_2 is effective in increasing T_c of Nd123. The Nd123 melt processed in PO_2 of 10^{-3} atm exhibited an unprecedented high onset T_c of 96 K with a sharp transition.

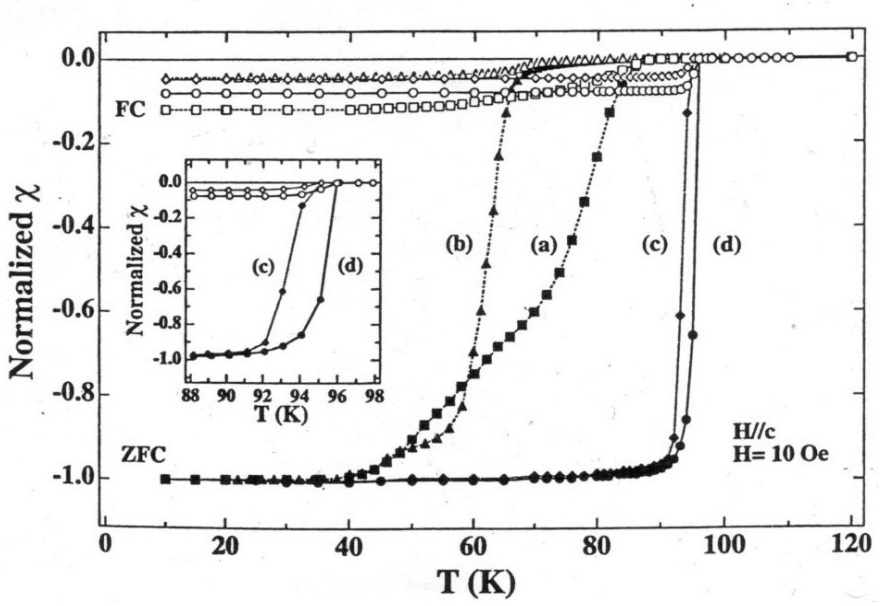

Fig. 1.11: Susceptibility $\chi(T)$ of Nd-Ba-Cu-O samples melt processed in (a) O_2, (b) Air, (c) 1 % O_2 in Air, and (d) 0.1 % O_2 in Air.

Fundamentally, the OCMG process is preferentially to stabilize the high T_c phase in the $RE_{1+x}Ba_{2-x}Cu_3O_{7-\delta}$ solid solution by utilizing a significant difference in their melting points in reduced oxygen atmosphere [32]. The OCMG process was also confirmed to be effective in obtaining not only high T_c but also strong flux pinning for other RE123 superconductors including Sm[36,37] and Eu[38] in addition to Nd and even for any combinations of three elements[39]. All these OCMG-processed RE123 were very promising since, in addition to an enhanced T_c of 94-96 K with a sharp transition, they exhibit large J_c values and high irreversibility field which are superior to those of Y123.

Muralidhar *et al*. also showed that the OCMG process assures high T_c in almost all the RE-123 systems like (Nd, Eu, Gd)$Ba_2Cu_3O_y$, (Nd, Sm, Gd)$Ba_2Cu_3O_y$, (Nd, Sm, Gd)$Ba_2Cu_3O_y$ and so on systems [40].

1. 6. 2 Flux pinning in RE-123 superconductors

RE-123 superconductors contain many types of defects such as twin planes, substitution regions, oxygen deficiency, cracks, dislocations, non-superconducting particle inclusions, stacking faults, etc., which all may act as pinning centers. To achieve higher J_c and irreversibility field B_i to improve the facilities of practical applications, it is very important to correctly understand the flux pinning mechanism in these RE-123 materials. Hence, in the followings subsections, the pinning by non-superconducting particles, pinning by lower-T_c and the pinning characteristics of the peak effect, an abnormal increase in the critical current density with increasing magnetic field, and the irreversibility field in RE-123 superconductors are described.

1. 6. 2. 1 Pinning by non-superconducting particles

The occurrence of the flux pinning interaction originates from the structure of the quantized flux line as shown in Fig. 1.6. That is, the superconducting order parameter, Ψ, has a zero point at the center of the flux line with a sharp variation within a range of the coherence length, ξ. Here, it disregards the anisotropy of the oxide superconductors, for simplicity. In addition, the magnetic flux is concentrated within a range of the penetration depth, λ, from the center. Hence, when the flux line moves in a part where the superconducting properties change spatially, it feels a change in the free energy which results in the flux pinning interaction. Because of a sharp variation in the structure of the order parameter (here it should be noted that ξ is much shorter than λ in oxide superconductors), this variation plays a dominant role in the flux pinning. Hence, only the pinning associated with the variation in Ψ is treated here. If it picks out the main terms at high fields, Eq. (1.6) is reduced to [41]

$$F_s = \frac{B_c^2}{\mu_0}\left[-|\psi|^2 + \frac{1}{2}\xi^2 \frac{(\nabla|\psi|^2)^2}{|\psi|^2}\right]. \qquad (1.12)$$

In the above, B_c is the thermodynamic critical field and $\psi = \Psi / |\Psi_\infty|$.

In the case of the pinning by non-superconducting particles such as 211 or 422 (the Nd-422 phase in Nd-123) phase particles, in the normal core of the flux line, $|\psi|$ is

small and $\nabla\psi$ is not zero. Hence, the energy is higher there because of the contribution of the two terms in Eq. (1.12). If the two cases of (a) and (b) are compared in Fig. 1.12, the energy is lower when the normal core meets the normal particle as in Fig. 1.12(a). When normal core meets with a normal precipitate, superconductivity is not destroyed the volume in which the normal core interact with normal precipitate, because, normal precipitate is normal conducting. This means that if the normal core meets a normal precipitate as in Fig. 1.12(a), the region with the higher energy density decreases, resulting in more favorable state in comparison with the case in Fig. 1.12(b). Since the normal core is almost in the normal state, the energy difference between the two situations, which is condensation energy, is given by

$$-(F_s - F_n)\times V. \tag{1.13}$$

In the above, F_s and F_n are the free energy density in the superconducting and normal states respectively, F_n-F_s is the condensation energy density, and V is the volume of cross-section of normal core with precipitate. Thus, it is seen that such normal precipitate works as an attractive pinning center. The condensation energy interaction is a pinning mechanism where the variation of condensation energy involved when the flux line is displaced and the pinning interaction arises.

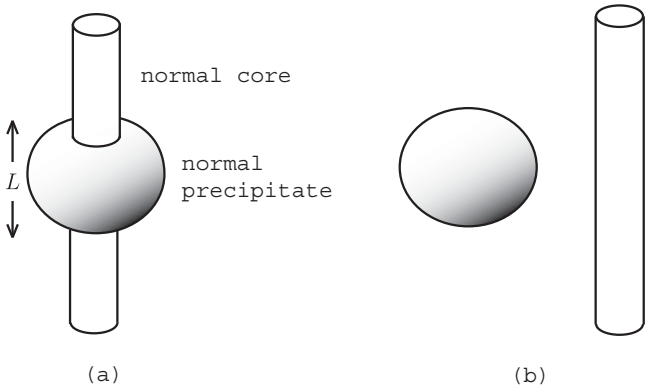

Fig. 1.12: Arrangement of normal core of flux line and normal precipitate.

At high fields where the order parameter is reduced due to an overlapping of normal cores of flux lines, the pinning energy decreases and the corresponding correction factor for the interaction force is

$$\left\langle |\psi|^2 \right\rangle \cong 1 - \frac{B}{B_{c2}}, \tag{1.14}$$

where $\langle ... \rangle$ represents the spatial average.

Hence, the pinning force density for the case of normal particle of size D and number

density N_p, after a simple calculation [42], is given by

$$F_p \cong \frac{\pi B_c^2 N_p D^2}{4\mu_0 a_f}\left(1-\frac{B}{B_{c2}}\right), \tag{1.15}$$

where a_f is the flux line spacing and it was assumed the local model for the structure of the normal core ($\Psi = 0$ within the range of ξ from the center), for simplicity. To be precise, the condensation energy interaction is overestimated in this case in comparison with the correct calculation, while the contribution from the kinetic energy is neglected. However, the result is fairly correct in spite of the simple approximation. This predicts that the pinning force density is proportional to the effective surface area of normal particles, N_pD^2, contained in a unit volume of the superconductor. That is,

$$F_p \propto N_p D^2 \tag{1.16}$$

On the other hand, the pinning force density is predicted to depend on temperature and magnetic field as

$$F_p(B,T) \propto B_{c2}^{3/2} B^{1/2}\left(1-\frac{B}{B_{c2}}\right) \tag{1.17}$$

where, it assumed that $B_c(T) \propto B_{c2}(T)$. At low fields and low temperatures where the effect of flux creep can be safely disregarded, Eq. (1.17) is reduced to

$$F_p(B,T) \propto \left[1-\left(\frac{T}{T_c}\right)^2\right]^{3/2} B^{1/2}, \tag{1.18}$$

where it assumed that $B_{c2}(T) \propto 1-(T/T_c)^2$.

In the case of 211 particles in Y-123 superconductor, the proportionality given by Eq. (1.16) was confirmed by Murakami *et al.* [43].

1. 6. 2. 2 Pinning by lower-T_c region

The superconducting properties in the substituted region or the oxygen-deficient region are: (a) lower critical temperature (T_{sc}); (b) smaller upper critical field (B_{sc2}); and (c) longer coherence length (ξ_s) than the values for the matrix [46]. It should be noted that the pinning property of these regions essentially depends on whether there is a proximity effect between these regions and the superconducting matrix. Since a superconducting tunneling current was observed even through a thick non superconducting Pr-123 layer in an Y-123/Pr-123/Y-123 junction and the typical size of

the lower-T_c is speculated to be of the order of a few tens of nm, the occurrence of the proximity effect in this regions seems to be plausible. Hence, both cases will be considered here.

In the case of no proximity effect, the lower-T_c region becomes normally conducting for temperature above T_{sc} and for magnetic field above B_{sc2}. Hence, the pinning mechanism is the same as that of normal particles and this region acts as a strong attractive pinning center. For $T < T_{sc}$ and $B < B_{sc2}$ this region is weakly superconducting. Hence, when this flux line meets this region, the flux line gains negative condensation energy, while the kinetic energy is enhanced. As a result, the flux pinning strength is speculated to be weak due to the offset. On the other hand, the substituted regions become normal state at high fields and those may contribute strongly to the flux pinning (see Fig. 1.13) [48]. Thus, this scenario explains the peak effect just on the basis of the elementary pinning mechanism, i.e., the field-induced (or temperature-induced) pinning mechanism [48].

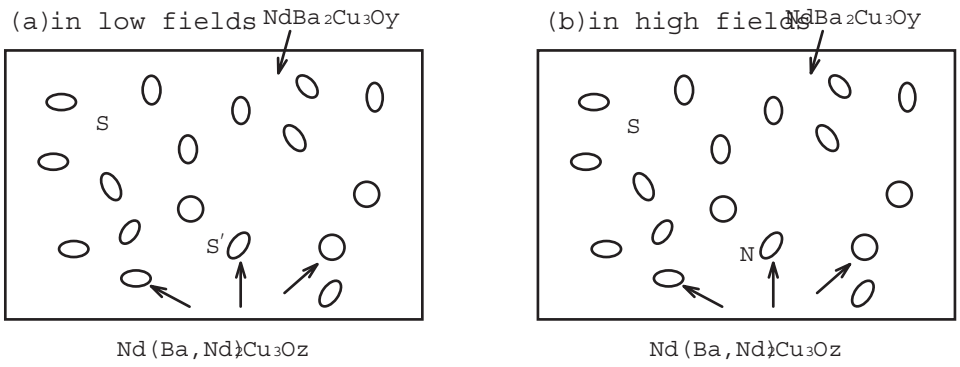

Fig. 1.13: Schematic illustration of field-induced flux pinning by finely distributed Nd-rich Nd-123ss regions (Fig. 22 of ref. 48).

Now it can be considered the case of the presence of the proximity effect. At temperature below T_{sc}, the lower-T_c region is in a weakly superconducting state. That is,

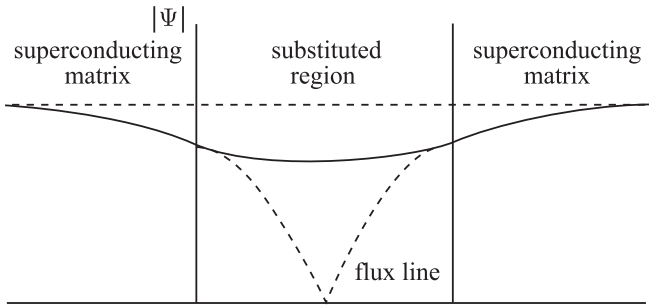

Fig. 1.14: Spatial variation of the order parameter around the lower-T_c region. The broken line represents the order parameter when a flux line exists in the lower-T_c region.

it is intrinsically in the superconducting state for $B < B_{sc2}$ and so, due to the proximity effect, also for $B > B_{sc2}$. In these cases, therefore, the flux pinning strength in this phase is speculated to be weak for the same reason as in the above case. On the other hand, for $T > T_{sc}$ the effective coherence length of the lower-T_c region, ξ_s, is very long. In fact, ξ_s diverges at $T = T_{sc}$. Hence, when the flux line comes in the lower-T_c region, the kinetic energy increases substantially due to the variation in the order parameter as shown in Fig. 1.14, resulting in a strong repulsive pinning. To be more exact, it is considered that this pinning mechanism becomes dominant at temperature just below T_{sc} at which ξ_s starts to become very long. It should be noted that the peak effect is not directly derived from this elementary pinning mechanism. That is, the elementary pinning force does not show drastic change but decreases monotonically with the increasing magnetic field. In the high field region where the flux line spacing, a_f, becomes comparable to the spacing of the lower-T_c region, the flux lines always exist in each lower-T_c region during their displacement driven by the Lorentz force. Hence, kinetic energy becomes very large as long as the superconductivity exists in this region. As a result, the superconductivity in the lower-T_c region is considered to disappear to avoid such an enhancement of the kinetic energy. At the same time the superconductivity in the surrounding higher-T_c matrix is also degraded due to the proximity effect. This is the same mechanism as the degradation of B_{c2} in Nb-Ti with artificially introduced Nb pins [47].

1.6.3 The flux pinning characteristics of the peak effect and the irreversibility field in RE-123 superconductors

The peak effect, an abnormal increase in the critical current density with increasing magnetic field, is sometimes seen in high-temperature superconductors. Typical

examples are that in Bi-2212 single crystals at very weak magnetic fields in the low temperature region and that in RE-123 single crystal or bulk specimens at medium fields in the medium temperature region.

For the explanation of the peak effect in RE-123 superconductors, two mechanisms have been proposed: the elementary field-induced pinning [48] and the order-disorder transition [49] of flux lines. The field-induced mechanism is already discussed in the previous section. In the case of order-disorder transition, it has been proposed that the increase of J_c with magnetic field is ascribed to the transitional change from an ordered state of flux lines with a weak pinning force to a disordered state with a strong pinning force. That is, the increase of J_c is attributed to a rearrangement of flux lines so as to fit to randomly distributed pinning centers initiated by the order-disorder transition in the flux line lattice. The corresponding movement of flux lines at the rearrangement is considered to be the shear (see Fig. 1.15(c)), and a softening of the shear modulus C_{66} is considered to take place at the order-disorder transition.

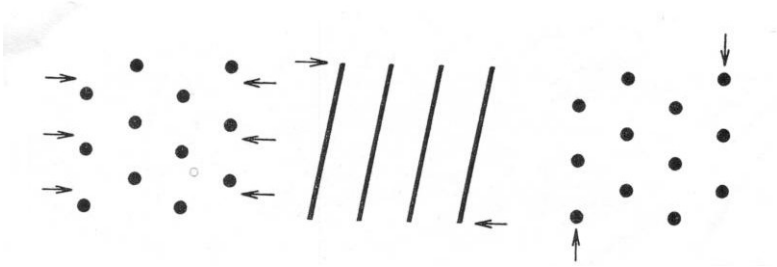

(a) (b) (c)

Fig. 1.15: (a) Uniaxial compression, (b) bending deformation and (c) shearing deformation.

It is known that the transition is determined by the elastic energy and the pinning energy. One of the features of this transition is the peak effect of critical current density in a magnetic field parallel to the *c*-axis. It is proposed that a double potential well is formed by a combination of the elastic energy and the pinning energy, as shown in Fig. 1.16.

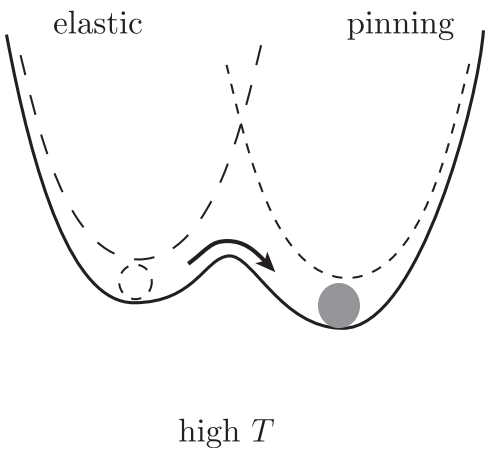

Fig. 1.16: Free energy composed of elastic energy and pinning energy: a double potential well with two stable states in the region of dimensional crossover of flux lines.

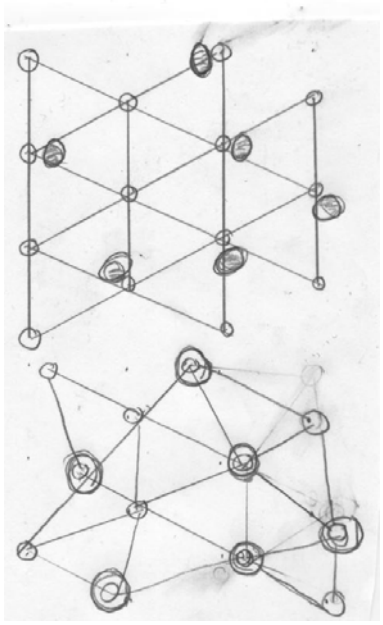

Fig. 1.17: Upper Figure is an order state and lower Figure is a disorder state which are shown schematically.

It is found in the peak effect that the critical current density changes discontinuously with magnetic field. In the case of this transition, there are two stable states with different values of the critical current density under the same conditions of temperature and magnetic field. This proves that this transition is first order. One of the two states is a state where flux lines are slightly deformed and weakly pinned as depicted as in the

upper Fig. 1.17. This state continues from a lower magnetic field. The other state is a state where flux lines are significantly deformed and strongly pinned and is attained at a higher magnetic field, which is shown schematically in the lower Fig. 1.17.

On the other hand, it was found [50-52] that J_c decreased in the medium field region and the peak effect disappeared by addition of 211 phase particles to Y-123 and Nd-123 superconductors. That is, the reduction in J_{cp} is ascribed to the interference between the repulsive pinning of lower-T_c regions and the attractive pinning of 211 particles, suggesting that the pinning mechanism of lower-T_c regions is not based on the field-induced pinning mechanism. The expected mechanism of lower-T_c regions is the repulsive kinetic energy interaction under the proximity effect [53].

On the other hand, the irreversibility field, the magnetic field at which the critical current density is reduced to zero and can be explained by the flux creep theory [54], depends on the flux pinning strength. It was found in Nd-123 [65] that irreversibility field B_i shifts to higher fields with increasing Nd-422 particles, indicating that Nd-422 are effective in enhancing B_i. The enhancement in B_i by adding 211 particles can also be found in Y-123 [55-57]. These results are consistent with the results [58] that J_c values in the high field region are increased with increasing V_f/d, where V_f is the volume fraction and d is the average diameter of 211 particles. Hence, it can be concluded that the pinning mechanism of the irreversibility field and that of the peak effect are different in Y-123 or Nd-123. In fact J_{cp} is likely to decrease while B_i tends to increase by addition of 211 or 422 phase in these superconductors. At high fields every flux lines can not occupy its preferred position and this leads to enhancement of kinetic energy interaction. Hence, the proximity effect ceases to avoid the enhancement of the proximity effect. Thus, J_c is determined only by the condensation energy interactions from 211 phases, and addition of 211 particles does not reduce B_i.

For practical applications, it is required to improve peak critical current density J_{cp} and B_i of bulk superconductors. Recently, Muralidhar *et al*. has developed new $Nd_{0.33}Eu_{0.33}Gd_{0.33}Ba_2Cu_3O_y$ called NEG-123 system and it has been systematically demonstrated that the flux pinning properties of the new material are superior to those of Y-123 or Nd-123.

Combination of three light rare earth elements in the elementary cell provides an exceptional technological freedom that enables to control a variety of physical characteristics of the final products. First of all, one can choose a combination of RE elements among several ones as shown in Fig. 1.18 [70]. It has been proved that all these elements fit well together and could be combined in the whole range of chemical

ratio. As a result, a largest J_c value of 5×10^8 A/m^2 at 77 K and 2 T was achieved in (Nd, Eu, Gd)-123 superconductors.

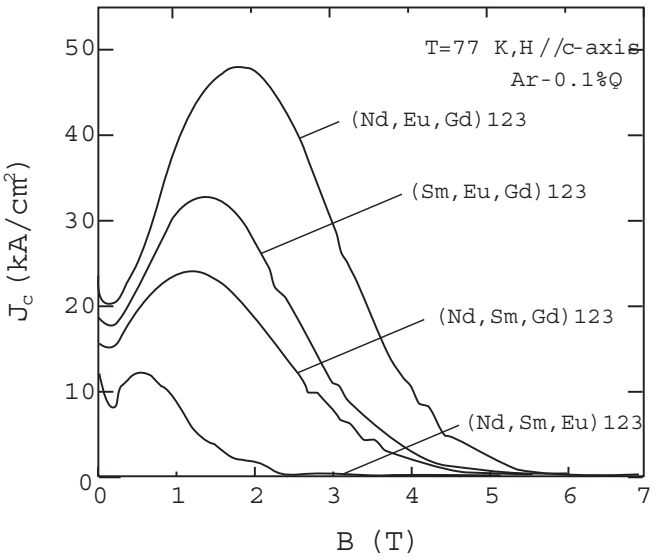

Fig. 1.18: J_c-B properties (77 K, $B \parallel c$-axis) of (R1, R2, R3)-123 composites OCMG processed in 0.1% O_2-Ar. This is Fig.1 of ref. [70]

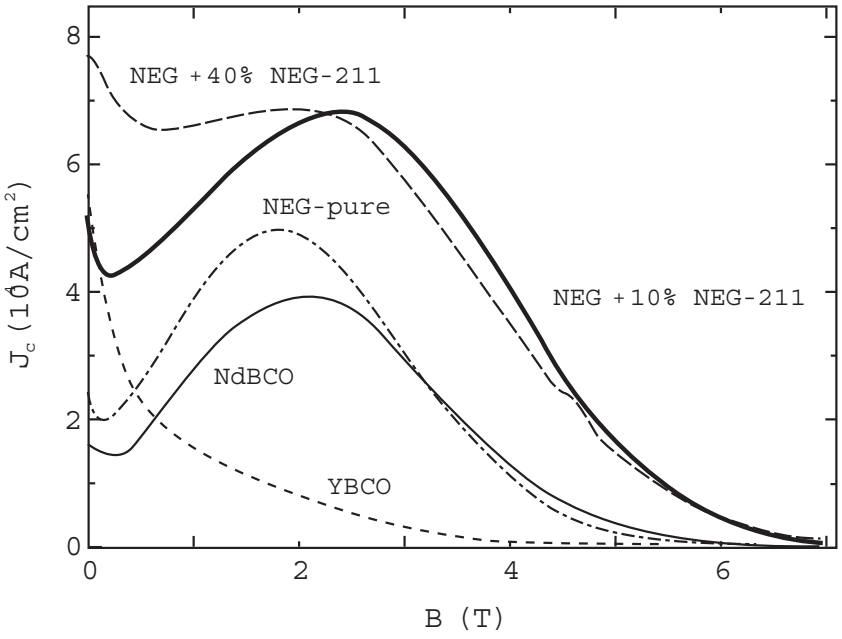

Fig. 1.19: Comparison of the field dependence of the critical current densities at 77 K measured by SQUID magnetometry; the field is applied parallel to the *c*-axis. This is Fig. 1 of ref. [71].

The critical current density, J_c, in bulk superconductors of the type $Nd_{0.33}Eu_{0.33}Gd_{0.33}Ba_2Cu_3O_y$ (NEG), where three rare earth elements (RE) are mixed together at the rare earth site, is considerably improved with addition of 211 phase particles [71]. That is, J_c is improved to the level of 7×10^8 A/m^2 in NEG-123 with 40 mol% NEG-211 at 77 K, at 2T, as shown in Fig. 1.19, together with data of melt-processed YBCO(Y-123) and NdBCO(Nd-123) superconductors.

Another advantage is a high compatibility of secondary phases with various ternary RE matrix. This enabled a wide manipulation with pinning characteristics. Muralidhar *et al*. [73] observed the enhancement of J_{cp} and B_i at 77.3 K in $Nd_{0.33}Eu_{0.33}Gd_{0.33}Ba_2Cu_3O_y$ superconductors with addition of 10-40 mol% NEG-211 secondary phase. They found that J_{cp} increased and B_i also almost increased with increasing NEG-211 phase: a large J_{cp} of 7×10^8 A/m^2 at B = 2.3 T and B_i over 7 T were achieved by addition of 40 mol% NEG-211 phase. Later, they measured [72] J_c-B properties at 77.3 K in $Nd_{0.33}Eu_{0.33}Gd_{0.33}Ba_2Cu_3O_y$ superconductors with addition of various 211 phases, i.e., NEG-211, EG-211, Eu-211 and Gd-211 of 0-50 mol% as shown in Fig. 1.20. In these measurements, J_{cp} almost increased with increasing volume fraction of various 211 phases, and B_i increased up to a maximum value at certain mol% of 211 phase and then decreased. The maximum B_i depended on the kind of 211 phase and their amounts. Thus, the behaviors of J_{cp} and B_i with addition of 211 phase in the new superconductors are complicated.

A control of the Nd:Eu:Gd ratio in the NEG-123 matrix is an effective way in tailoring the pinning properties of this compound. A proper choice of the Nd: Eu: Gd ratio leads to control of the peak position between 1 and 4 T at 77 K as shown in Fig. 1.21 [74]. The maximum pinning effect in a broad field range can be achieved by combining the optimum concentration of 211 phase particles with the optimum chemical ratio in the matrix.

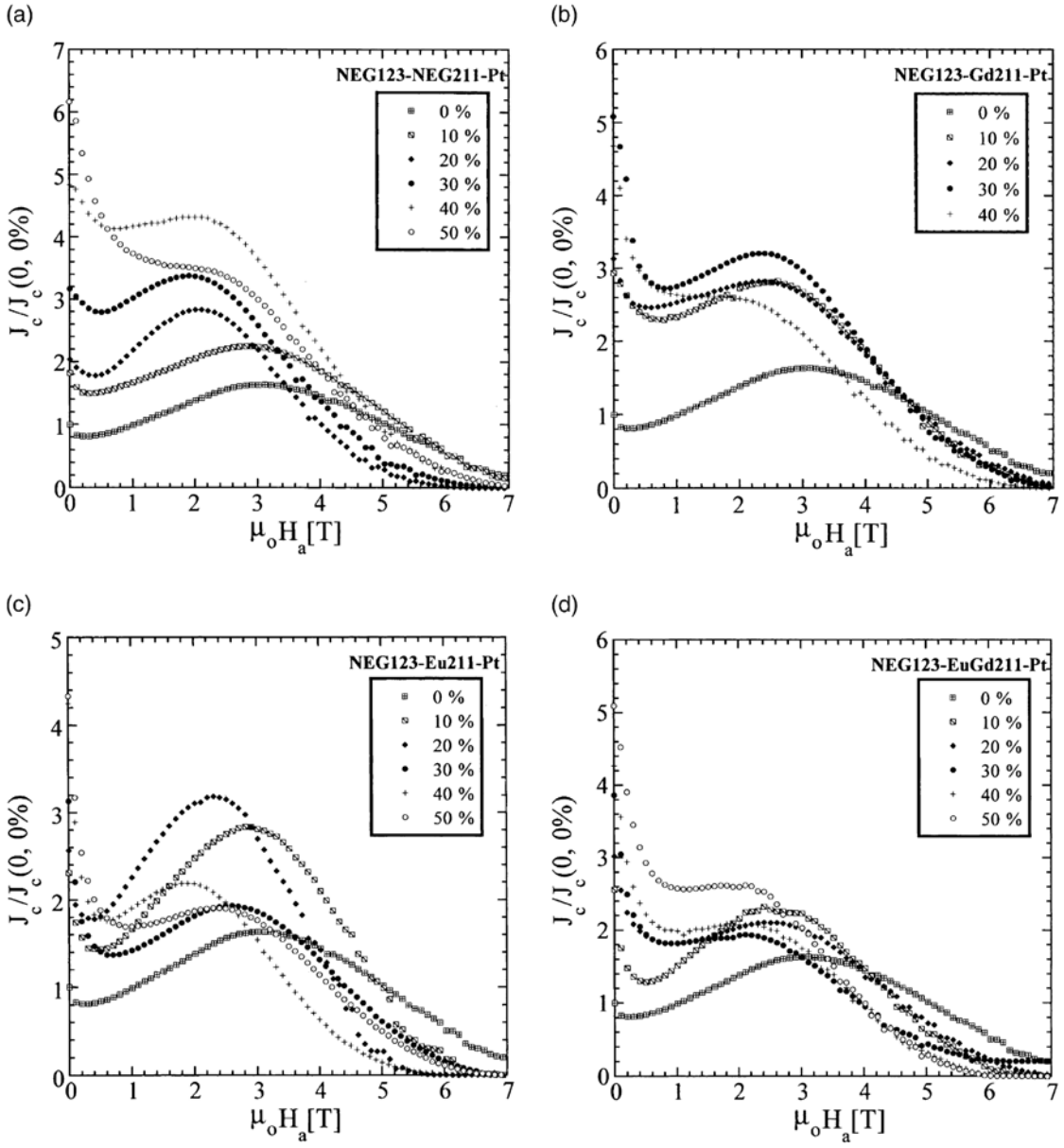

Fig. 1.20: Field dependence of J_c obtained from magnetization measurements at T=77 K ($B \parallel c$-axis) for NEG superconductors with different volume fractions of (a) NEG-211 phase, (b) Gd-211 phase, (c) Eu211 phase, and (d) (Eu, Gd)-211 phase. Note that the shape of the Jc-B curves depends on the secondary phase type and amount. This is Fig. 3 of ref. 72.

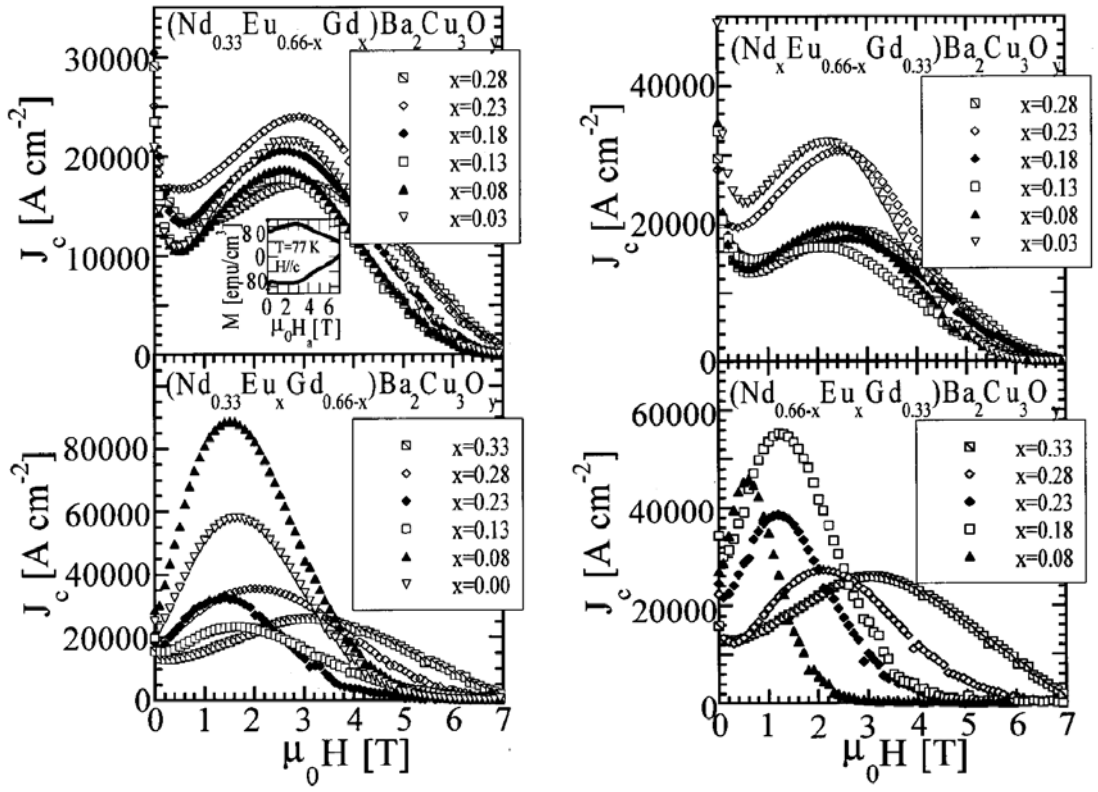

Fig. 1.21: Field dependence of the critical current density (T = 77 K, Ha parallel to the c-axis) for NEG-123 samples with varying Eu/Gd contents. This is Fig. 1 of ref. 74.

Figure. 1.22 shows the field dependence critical current density in newly developed $(Nd_{0.33}Eu_{0.38}Gd_{0.28})Ba_2Cu_3O_y$ sample with 5 mol% NEG-211, together with data of melt-processed YBCO sample and $(Nd_{0.33}Eu_{0.33}Gd_{0.33})Ba_2Cu_3O_y$ sample [75]. Characteristically, the melt-processed YBCO(Y-123) sample does not exhibit the peak effect with the irreversibility field around 4 T. OCMG processed NEG-123 sample with the matrix ratio of 1:1:1 shows a clear peak effect at 2 T accompanied by a high irreversibility field around 6 T. The most remarkable feature of the newly developed NEG-123 sample with the matrix ratio of 1: 1.25: 0.85 is that the irreversibility field was over 14 T and the peak critical current density was about 7×10^8 A/m^2 at around 4.5 T. This is the highest peak position and largest irreversibility field reported so far for RE-123 superconductors at this temperature.

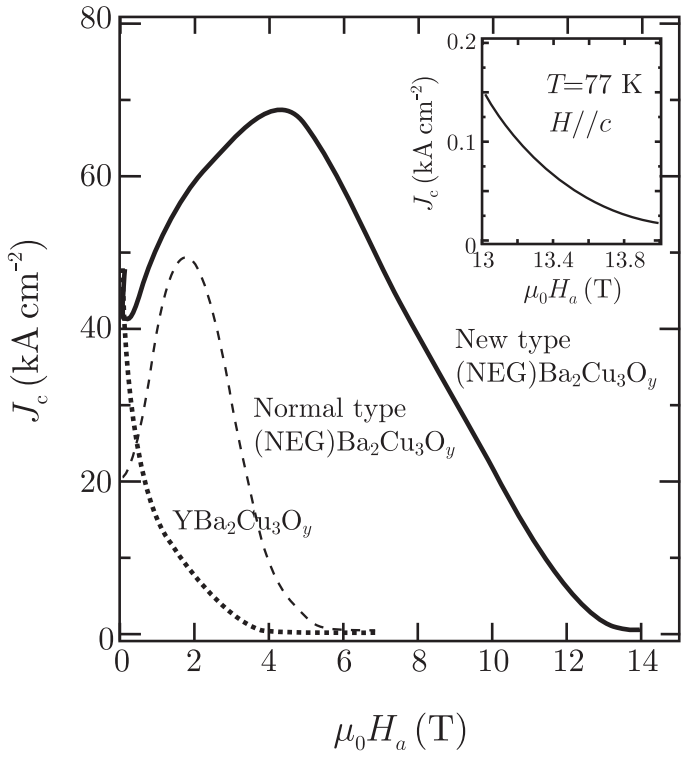

Fig. 1.22: Comparison of the field dependence of the critical current density (T = 77 K and H_a // c-axis) for melt-processed YBCO, OCMG processed $(Nd_{0.33}Eu_{0.33}Gd_{0.33})Ba_2Cu_3O_y$ sample and newly developed $(Nd_{0.33}Eu_{0.38}Gd_{0.28})Ba_2Cu_3O_y$ sample with 5 mol% NEG-211. Note the new NEG sample exhibits high critical current density (J_c) of 7×10^8 A/m^2 at the peak around 4.5 T at 77 K. The inset shows that the irreversibility field exceeds 14 T. This figure was in the Fig. 3 in ref. 75.

It was found that the pinning performance could be tailored in NEG-123 by controlling chemical ratio of Nd, Eu and Gd elements together with addition of 211 phase. Therefore, in the present study, we focus on the most promising $Nd_{0.33}Eu_{0.38}Gd_{0.28}Ba_2Cu_3O_y$ superconductor which shows a high performance at high fields and study the variations of J_{cp} and B_i with volume fractions of 211 phase to find out the mechanisms which determine the peak effect and B_i.

1. 7 The transverse flux bundle size

The volume of flux bundle is estimated from the size of flux bundle in transverse direction R given by

$$R = \left(\frac{C_{66}}{\alpha_{\mathrm{L}}} \right)^{1/2}, \qquad (1.19)$$

as shown in Fig. A4(b) in the Appendices (flux creep-flow model). Here α_{L} is the Labusch parameter. The shear modulus of flux lines, C_{66}, is largely dependent on the condition of flux line lattice. In the case of perfect triangular lattice in three dimensional, C_{66} takes maximum value of C_{66}^{0}, and it is given by [73]

$$C_{66}^{0} = \frac{B_{\mathrm{c}}^{2} B}{4\mu_0 B_{\mathrm{c2}}} \left(1 - \frac{B}{B_{\mathrm{c2}}} \right)^{2}, \qquad (1.20)$$

and decreases with disorder of flux line lattice, then reaches to zero when flux line lattice is in melt condition.

It is considered that transverse flux bundle size, *R*, is of the order of a_{f} of several times larger except the case of very weak pinning of superconductor. In the case of very strong pinning force, *R* is smaller than a_{f}. Although, the size is not smaller than flux line spacing, *R* is expresses as

$$R = g a_{\mathrm{f}}, \qquad (1.21)$$

where $g^{2} (\geq 1)$ is the number of flux lines in the flux bundle. Therefore, g^2 is given by

$$g^{2} = \frac{C_{66}}{\zeta J_{\mathrm{c0}} B a_{\mathrm{f}}}. \qquad (1.22)$$

where ζ is a constant depended on the kind of pinning center and J_{c0} is virtual critical current density in the ideal flux creep free case.

For the case of three dimensional perfect triangle flux line lattice, g^2 takes maximum value, g_{e}^{2}, and it is given by[74]

$$g_{\mathrm{e}}^{2} = \frac{C_{66}^{0}}{\zeta J_{\mathrm{c0}} B a_{\mathrm{f}}}. \qquad (1.23)$$

As abovementioned, the value of C_{66} is largely dependent on the condition of flux line lattice and changes from maximum value of C_{66}^{0} to zero, and there is no straightforward method to determine the flux bundle size. Therefore, it is assumed based on the principle of minimization of energy dissipation that g^2 is determined so as to achieve maximum critical current density under flux creep [63]. According to the theory [63], g^2 is given as

$$g^2 = g_e^2 \left[\frac{5k_B T}{2U_e} \log\left(\frac{Ba_f \nu_0}{E_c} \right) \right]^{4/3}, \quad (1.24)$$

where ν_0 is the attempt frequency of the flux bundle, k_B is the Boltzmann constant, U_e is the pinning potential at $g = g_e$ and E_c is the criteria of electric field, respectively. From the relationship of $U_e \propto g_e$, we have

$$g^2 \propto g_e^{2/3}. \quad (1.25)$$

When the size of a bulk superconductor is larger than the size of flux bundle in longitudinal direction L and transverse direction R, the volume of flux bundle is given by

$$V = LR^2, \quad (1.26)$$

and the pinning potential is given by

$$U_0 = \frac{0.835 g^2 k_B J_{c0}^{1/2}}{\zeta^{3/2} B^{1/4}}. \quad (1.27)$$

On the other hand, if the thickness of the superconductor d is smaller than L as in a thin film, V is given by

$$V = dR^2, \quad (1.28)$$

and U_0 is given by

$$U_0 = \frac{4.23 g^2 k_B J_{c0} d}{\zeta B^{1/2}}. \quad (1.29)$$

Hence, the reduction in the flux bundle size is more prominent for the case of magnetic field parallel to the c-axis, suggesting that the effect of flux creep is more severe in this case. In conclusion that the flux pinning should be made stronger to enhance U_0. The strengthening of flux pinning surely makes g^2 small. However, g^2 never takes a value smaller than 1, and hence, if the flux pinning is made stronger beyond some level, it reflects directly to the enhancement of U_0.

1. 8 Scope of this thesis

Among high-temperature superconductors, RE-123 is one of the most interesting materials to study its pinning properties, as it is considered to be a strong candidate for practical applications. In single crystal RE-123 superconductors, it has been reported that the critical current density J_c has a broad peak due to the pinning of a low T_c phase in which RE sites are substituted by Ba [64, 65]. Recently, it has been also reported that the superior performance of higher peak critical current density J_{cp} and irreversibility field B_i in NEG-123 bulk superconductors at 77.3 K as compared to Y-123 or Nd-123

[66-69]. However, further improvement is still needed for facilitating applications. To achieve the higher J_{cp} and B_i, it is necessary to understand the flux pinning mechanisms which brings about high J_{cp} and B_i, which is the main objective of this thesis.

In chapter two, sample preparation of the flux grown $NdBa_2Cu_3O_y$ single crystal superconductor and $(Nd_{0.33}Eu_{0.38}Gd_{0.28})Ba_2Cu_3O_y$ bulk superconductors with addition of 211 phase particles, experimental procedures and equipments employed in this study are briefly described.

In chapter three, the relation between the apparent pinning potential U_0^* and the critical current density J_c is investigated to find out the mechanism of the peak effect in a single crystal $NdBa_2Cu_3O_y$ superconductor. For comparison with theoretical results, the flux creep-flow model is used, and the behavior of the parameter g^2, A_m and σ^2 is argued to clarify the mechanism of the peak effect.

In chapter four, a focus is given on the most promising $(Nd_{0.33}Eu_{0.38}Gd_{0.28})Ba_2Cu_3O_y$ superconductors which shows a high performance at high fields and studied the variation of peak critical current density J_{cp} and B_i with the volume fraction of 211 phase to find out the mechanisms which determine the peak effect and B_i.

In chapter five, the conclusion regarding the influence of the flux pinning in NEG-123 superconductors is described.

References

1. H. Kamerlingh Onnes, *Leiden Commun*. **120b, 122b, 124c** (1911)
2. W. Meissner and R. Ochsenfeld, *Naturwissenschaften* **21**, 787 (1933)
3. B. D. Josephson, *Phys. Lett*. **1,** 251 (1962)
4. P. W. Anderson and J. M. Rowell, *Phys. Rev. Lett*. 10, 230 (1963)
5. J. G. Bednorz and K. Muller, *Z. Phys.* B**64**, 198 (1986)
6. M. K. Wu, J. R. Ashburn, C. J. Torng, P.H. Hor, R. L. Meng, L. Gao, Y. Q. Wang and C. W. Chu, *Phys. Rev. Lett.* **58**, 908 (1987)
7. H. Maeda, Y. Tanaka, M. Fukutomi and T. Asano, *Jpn. J. Appl. Phys*. **27**, L209 (1988)
8. S. S. P. Parkin, V. Y. Lee, E. M. Engler, A. I. Nazzal, T.C. Huang, G. Gorman, R. Savoy and R. Beyers, *Phys. Rev. Lett*. **60**, 2539 (1988)
9. A. Schilling, M. Cantoni, J. D. Guo, and H. R. Ott, *Nature* **363**, 56 (1993)
10. L. Gao, Y. Y. Xue, F. Chen, Q. Xiong, R. L. Meng, C. W. Chu, J. H. Eggert, and H. M. Mao, *Phys. Rev.* B **50**, 4260 (1993)
11. V. L. Ginzberg and L. D. Landau, *Zh. Eksp. Teor. Fiz*. **20**, 1064 (1950)
12. F. C. Moon, P. Z. Chang, *Appl. Phys. Lett*. **56**, 22 (1990)
13. K. Salama, V. Selvamanickam, L. Gao, K. Sun, *Appl. Phys. Lett*. **54**, 2352 (1989)
14. A. M. Campbell, D. A. Cardwell, *Cryogenics* **37**, 567 (1997)
15. M. Muralidhar, M. Jirsa, N. Sakai, M. Murakami, *Supercond. Sci. Technol.* **15**, R1 (2002)
16. K. Yokoyama, T. Oka, H. Okada, K. Noto, *Physica C*, **392-396**, 739 (2003)
17. S. Wang, *et. al*, *IEEE Trans. Applied Superconductivity,* **13**, 2134 (2003)
18. M. Murakami, *Supercond. Sci. Technol.*, **5**, 185 (1992)
19. R. Weistein, I. G. Chen, J. Liu, J. Xu, Y. Obot, C. Foster, *J. Appl. Phys*., **73**, 6533 (1993)
20. J. R. Hull, *Supercond. Sci. Technol*., **13**, R1 (2001)
21. T. Ohara, H. Kumakura, H. Wada, *Physica C,* **13**, 1272 (2001)
22. A.C. Day, et al., *Supercond. Sci. Technol.*, **15**, 838 (2002)
23. S. Tanaka, *Physica C*, **392-396**, 1 (2003)
24. See for example, G. Xiao, F. H. Treitz, A. Gavrin, and G. L. Chien, *Solid State Commun.*, **63**, 817 (1987); P. H. Hor, R. L. Meng, Y. Q. Wang, L. Gao, Z. J. Huang, J. Bechtold, K. Forster, and C. W. Chu, *Phys. Rev. Lett*., **58**, 1891 (1987); S. Kanbe, T. Hasegawa, M. Aoki, T. Nakamura, H. Koinuma, K. Kishio, K.

Kitazawa, H. Takagi, S. Uchida, S. Tanaka, K. Fueki, *Jpn. J. Appl. Phys*. **26**, L815 (1987); T. P. Oriando, K. A. Delin, S. Foner, E. J. McNiff Jr, J. M. Tarascon, L. H. Greene, W. R. Mckinnon, and G. W. Hull, *Phys. Rev.* B **36**, 2394 (1987)

25. J. M. Tarascon, L. H. Greene, B. G. Bagley, W. R. Mckinnon, P. Barboux, and G. W. Hull, in *Novel Superconductivity* (ed. S. A. Wolf and V. Z. Kresin), Plenum, New York, 7054 (1987)
26. S. Jin, T. H. Tiefel, R. C. Sherwood, M. E. Davis, R. B. van Dover, G. W. Kammlott, R. A. Fastnacht and H. D. Keith, *Appl. Phys. Lett.* **52**, 2074 (1988)
27. K. Salama, V. Selvamanickam, L. Gao and K. Sun, *Appl. Phys. Lett*. **54**, 2352 1989
28. M. Murakami, *Mod. Phys. Lett*. B **4**, 163 1990
29. M. Murakami, S. Gotoh, H. Fujinoto, K. Yamaguchi, N. Koshizuka and S. Tanaka, *Supercond. Sci. Technol.* **4,** S49 1991
30. L. Zhuo, P. Zhang, P. Ji, K. Wang, J. Wang and X. Wu, *Supercond. Sci. Technol.* **3**, 490 1990
31. D. Shi, S. Sengupta, J. S. Lou, C. Varanasi and P. J. McGinn, *Physica C* **213**, 179 1993
32. S. Hu, H. Hojiaji, A. Barkatt, M. Boroomand, M. Hung, A.C. Buechele, A. N. Thorpe and D. Davis, HTS Material, *Bulk Processing and Bulk Applications* ed C. W. et al Singapore: World Scientific 313 1992
33. S. I. Yoo and R. W. McCallum, *J. Mat*. **41**, 50 1989
34. M. Murakami, *Supercond. Sci. Technol*. **5**, 185 1992
35. S. I. Yoo, N. Sakai, H. Takaichi, T. Higuchi and M. Murakami, *Appl. Phys. Lett.* **65**, 633 1994
36. S. I. Yoo, N. Sakai, T. Higuchi, M. Murakami and S. Tanaka, *Jpn. J. Appl. Phys.* **33**, L1000 1994
37. S. I. Yoo, N. sakai, T. Higuchi, and M. Murakami, *IEEE Trans. Appl. Supercond.* **5**, 1568 1995
38. M. Murakami, S. I. Yoo, T. Higuchi, T. Oyama and N. Sakai, *Proc. 1994 Topical Int. Cryogenic Materials Conf. Singapore*: World Scientific 52 1995
39. T. Saitoh, K. Segawa, K. Kamada, N. Sakai, S. I. Yoo and M. Murakami "*The 1995 Int. Workshop on Superconductivity Hawaii*," *18-27 June 1995*, 330 1995
40. M. Muralidhar, M. Jirsa, N. Sakai and M. Murakami, *Supercond. Sci. Technol.* **16** R1 (2003)

41. T. Matsushita, *Proc. 8th Int. Workshop on Critical Currents in Superconductors* (Singapore: World Scientific) 63 (1996)
42. T. Matsushita, E. S. Otabe, B. Ni, K. Kimura, M. Morita, M. Tanaka, M. Kimura, K. Miyamoto and K. Sawano, *Jpn. J. Appl. Phys.* **30** L342 (1991)
43. M. Murakami, H. Fujimoto, K. Yamaguchi, N. Nakamura, N. Koshizuka and S. Tanaka, *J. Adv. Sci*. **4** 75 (1992)
44. M. Murakami, S. Gotoh, N. Koshizuka, S. Tanaka, T. Matsushita, S. Kambe and K. Kitazawa, *Cryogenics* **30** 390 (1990)
45. M. Murakami, K. Yamaguchi, H. Fujimoto, N. Nakamura, T. Taguchi, N. Koshizuka and S. Tanaka, *Cryogenics* **32** 930 (1992)
46. T. Matsushita, *Supercond. Sci. Technol*. **13,** 730, (2000).
47. T. Matsushita, M. Iwakuma, K. Funaki, K. Yamafuji, K. Matsumoto, O. Miura and Y. Tanaka, *Advances in Cryogenic Engineering*, **42** 1103 (1996)
48. M. Murakami, N, Sakai, T. Higuchi, S. I. Yoo, *Supercond. Sci. Technol.* **9**, 1015 (1996)
49. D. Ertas and R. D. Nelson, *Physica C* **272**, 79 (1996)
50. D. Yoshimi, M. Migita, E. S. Otabe, T. Matsushita, *Physica C* **357**, 590 (2001)
51. T. Matsushita, D. Yoshimi, M. Migita, E. S. Otabe, *Supercond. Sci. Technol*. **14**, 732 (2001)
52. T. Mochida, N. Chikumoto, T. Higuchi and M. Murakami, *Advance in Superconductivity* **10**, 489 (1998)
53. T. Matsushita, M. Iwakuma, K. Funaki, K. Yamafuji, K. Matsumoto, O. Miura and Y. Tanaka, *Advance in Cryogenic Engineering* **42**, 1103 (1996)
54. T. Matsushita T. Fujiyoshi, K. Toko and K. Yamafuji, *Appl. Phys. Lett*. **56**, 2039 (1990)
55. M. Murakami, S. Gotoh, H. Fujimoto, K. Yamaguchi, N. Koshizuka and S. Tanaka, *Supercond. Sci. Technol.* **4,** S43 (1991)
56. M. Murakami, H. Fujimoto, S. Gotoh, K. Yamaguchi, N. Koshizuka and S. Tanaka, *Physica C* **185-189**, 321 (1991)
57. P. J. Kung, M. P. Maley, M. E. McHenry, J. O. Willis, M. Murakami and S. Tanaka, *Phys. Rev.* B **48**, 13922 (1993)
58. T. Mochida, *Ph.D thesis* **Chapter 4**, 63 (2000)
59. M. Muralidhar, K. Segawa and M. Murakami, *Materials Science and Engineering* B **65**, 42 (1999)
60. M. Muralidhar, and M. Murakami, *Physica C* **363**, 19 (2001)
61. M. Muralidhar, N. Sakai, N. Chikumoto, M. Jirsa, T. Machi, M. Nishiyama , Y.

Wu and M. Murakami, *Phys. Rev. Lett.* **89**, 237001-1 (2003)
62. T. Matsushita, T. Fujiyoshi, K. Toko, K. Yamafuji, *Appl. Phys. Lett.*, **56**, 2039 (1990)
63. T. Matsushita, *Physica C,* **217**, 461 (1993)
64. M. Daumling, M. J. Seuntjens, C. D. Larbalestier, *Nature* 346, 332 (1990)
65. H. Suematsu, H. Okamura, S. Lee, N. Nagaya, H. Yamauchi, *Physica C* **338**, 96 (2000)
66. M. Muralidhar, M. R. Koblischka, T. Saitoh and M. Murakami, *Supercond. Sci. Technol*. **11,** 1349 (1998)
67. M. R. Koblischka, M. Muralidhar and M. Murakami, *Appl. Phys. Lett*. **73**, 2351 (1998)
68. A. K. Pradan, M. Muralidhar, M. R. Koblischka, M. Murakami, K. Nakao and N. Koshizuka, *Appl. Phys. Lett.* **75**, 253 (1999)
69. M. Muralidhar, M. R. Koblischka, P. Diko and M. Murakami, *Appl*. *Phys. Lett.* **76**, 91 (2000)
70. Muralidhar *et al*, *Physica C*, **282-287**,(1997),503.
71. Muralidhar *et al*. Phys. Stat. Sol. (a) **171**, R7 (1999)
72. M. Muralidhar and M. Murakami, *Physica C* **363**, 19, (2001)
73. M. Muralidhar, K. Segawa and M. Murakami, *Materials Science and Engineering* B**65**, 42, (1999)
74. M. Muralidhar, M. Jirsa, N. Sakai and M. Murakami, *Appl. Phys. Lett.* **79**, 3107, (2001)
75. M. Muralidhar, N. Sakai, M. Jirsa and M. Murakami, *IEEE. Trans. Appl. Superconductivity* **13**, 3091, (2003)

Chapter 2 Experimental Method

2. 1 Introduction

In this chapter, general experimental procedures and equipments employed in this thesis are briefly described. The details of sample preparation condition as well as the measurement conditions are described in the following subsections.

2. 2 Crystal Structure of $NdBa_2Cu_3O_y$ single crystal superconductor

Almost all HTSCs (High Temperature Superconductors) are complex layered copper-containing oxides whose structure contains oxygen-deficient perovskite blocks (Fig. 2.1) [1]. It is the CuO_2 layer that is currently considered to be responsible for superconductivity in cuprates. In these layers, the copper atoms form a square network, whereas the oxygen atoms are placed on the lines connecting copper [2,3]. The $3dx^2$-y^2 electrons of copper and 2*p* electrons of oxygen are delocalized in the layer, and such compounds possess a metallic type of conductivity. At temperatures below the critical temperature, superconductivity arises upon doping the CuO_2 layers with an optimum amount of charge carriers (Fig. 2.2) [1].

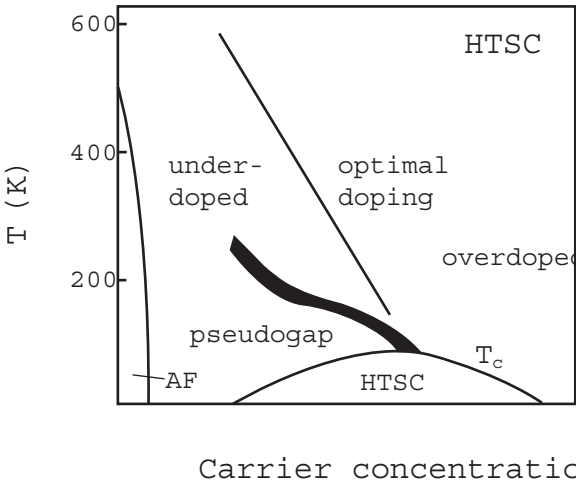

Fig. 2.1: Physical phase diagram of HTSC cuprates.

It was experimentally established that superconductivity requires that the formal oxidation state of copper in the CuO_2 layers be somewhat different from +2 and lie

within the range of +2.05.. + 2.25 for hole superconductors. The Cu-O bond length in the layer is yet another important parameter determining the superconducting properties; however, these bonds should be longer and exceed 0.22 nm.

In other words, the structure of superconducting cuprates contains inequivalent Cu-O bonds, viz., strong in-plane bonds and weaker perpendicular bonds.

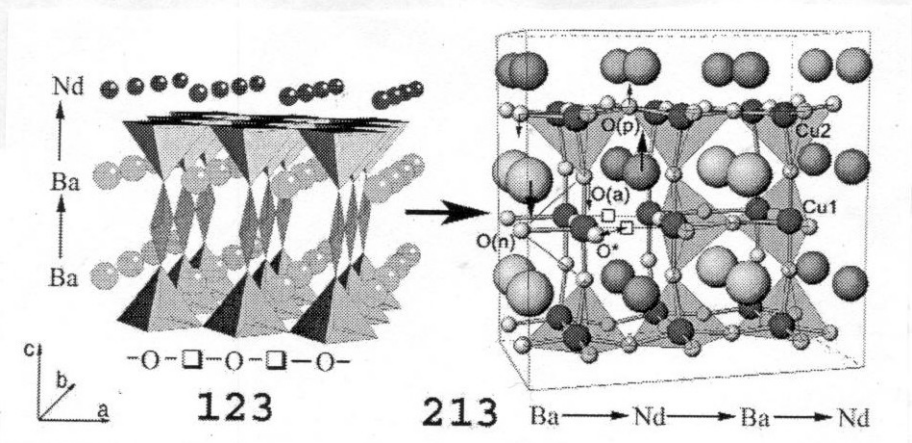

Fig. 2.2: Structure of the $Nd_{1+x}Ba_{2-x}Cu_3O_y$ solid solution with various types of cation and anion ordering. "123"stands for a solid solution (x = 0 and z = 7) with an ideal crystal structure and a high critical superconducting transition temperature T_c (a layer structure with ordered chains of oxygen atoms "O" and vacancies "□", left panel); "213" is a dielectric solid solution with x = 1, z = 7; O^* is a position with a varied oxygen occupancy.

As a consequence, HTSCs have a layered structure. Electrical neutrality requires the presence of other charge-compensating layers usually consisting of readily polarizable ions (e.g., Ba^{2+}) which, along with holes in the CuO_2 layer, help no form the Cooper pairs upon transition to the superconducting state.

In the case of $NdBa_2Cu_3O_y$ single crystal superconductor, the Nd-123 phase (Fig. 3.2) consists of superconducting (SC) and dielectric blocks. In terms of a structure description as alternate layers, the SC block is adequate to a Nd-vacancy layer flanked by two CuO_2 superconducting planes, the latter being oxygen-stoichiometric and concentrating holes. The charge-reservoir block is adequate to a Ba-O (apical oxygen) layer positioned between one superconducting plane and a CuO_{7-x} oxygen-deficient layer. Its saturation by oxygen generates alternate oxygen chains and vacancies in the CuO_{7-x} plane, results in a rhombic configuration around copper and gives rise a structure orthorhombicity, changes the copper oxidation number, and causes a charge transfer to

the SC planes.

In the structure of $Nd_{1+x}Ba_{2-x}Cu_3O_z$, neodymium substitutes for a part of barium in barium positions. Intermediate solid solution ($0.3<x<0.6$, "366") is tetragonal phase with disordered cation and anion sub lattices[3]. The solid solution of the 213 type (Fig. 2.2) is orthorhombic over its entire range of existence, including high temperatures [4-10], because of barium and neodymium ion ordering in barium positions[7,8]. A superstructure is formed, and the primitive cell of 123 type is doubled along the *c*-axis and in the normal direction giving a face-centered super cell. The appearance of alternate chains of barium and neodymium ions dictates oxygen ion reordering.

2. 3 Sample preparations

2. 3. 1 Flux-grown $NdBa_2Cu_3O_y$ single crystal superconductor

High purity commercial powders of Nd_2O_3, $BaCO_3$ and CuO were used as starting materials. They were weighted to have a nominal composition, and mixed thoroughly. The mixed powder was calcined at 870 ^{0}C for 24 h in air. The calcined powder was placed on a yttria-stabilized zirconia (YSZ; 3 mol% Y_2O_3 in ZrO_2) crucible. The materials were heated to a starting temperature (T_{start}) and slowly cooled to a finish temperature (T_{finish}) at the rate of 1 ^{0}C/h, then furnace cooled. A sealed furnace was used for this process. Oxygen annealing was carried out using a sealed tube furnace as illustrated in Fig. 2.3, which shows a schematic illustration of a temperature profile for the melt process. The sample is heated up to a target temperature (T_{high}), which is above

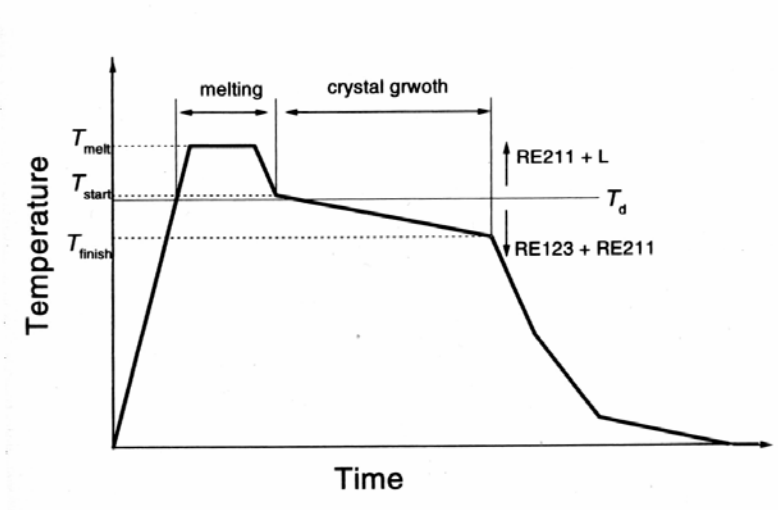

Fig. 2.3: Schematic illustration of temperature profile for melt-processing.

the peritectic decomposition temperature of RE123. After held for a fixed time, the sample is cooled to the temperature (T_{start}) at which the crystal growth startes followed by slow cooling. Pure oxygen gas is supplied from an oxygen cylinder at a flow rate of 300-500 ml/min. Samples were placed on a Pt foil, which was located at the center of the tube furnace. The preparation condition of flux-grown Nd-Ba-Cu-O is given in Table 2.1 [13]. The details of sample preparation conditions are described in ref. 11,12.

Table 2.1: The preparation conditions of flux-grown Nd-Ba-Cu-O [3].

Batch (No.)	Nd:Ba:Cu (Nominal composition)	Crucible	PO_2 (%)	T_{start} (^{0}C)	T_{finish} (^{0}C)
10	2:30:68	ZrO_2	1.0	1050	910
11	2:30:68	ZrO_2	0.1	1030	890

2. 3. 2 OCMG processed-(Nd, Eu, Gd)$Ba_2Cu_3O_y$ bulk superconductors with addition of 211 phase particles.

High-purity commercial powders of Nd_2O_3, Eu_2O_3, Gd_2O_3, $BaCO_3$ and CuO were mixed in quantities corresponding to a nominal composition of ($Nd_{0.33}$, $Eu_{0.38}$, $Gd_{0.28}$)$Ba_2Cu_3O_y$. The starting powders were thoroughly ground and calcined at 880^{0}C for 24h with intermediate grinding, then pressed into pellets. Sintering was carried out at 900^{0}C for 15h. This process was repeated three times under partial pressure (pO_2) of 0.1% O_2. Next, commercial Nd-422, Eu-211 and Gd-211 powders were mixed in the ratio 1:1:1 for preparing NEG-211 secondary phase particles and then, Eu-211 and Gd-211 were mixed in the same ratio for EG-211 phase particles. Then, volume fractions of 3, 7, 10 mol% of NEG-211 and 3, 5, 7, 10 mol% of EG-211 were added to the NEG-123 powders. 0.5 mol% of Pt was added for the secondary phase refinement, and also 10 wt% of Ag_2O for improvement of the mechanical properties. Finally, well-mixed [14] powders were pressed into pellets of 20 mm diameter and 15 mm thickness, which were consolidated by cold isostatic pressing with a pressure of 200 MPa. For differential thermal analysis (DTA) measurements, the powders were pre-treated at 925^{0}C in flowing Ar-0.1%O_2 for 15h. DTA measurements were performed under the same conditions to determine the peritectic decomposition temperature, T_p.

This temperature was then used to schedule the heat treatment profile of the oxygen controlled melt growth (OCMG) process. All the samples were fabricated with the OCMG process, under oxygen partial pressure 0.1% O_2 and gas flow rate of 300 ml/min. The details of the heat treatment schedule can be found elsewhere [15].

2. 4 DC magnetization measurements

2. 4. 1 General description of SQUID magnetometer

A commercial SQUID (superconducting quantum interference device) magnetometer (Quantum Design; MPMS-7) was used for DC magnetization measurements. The general feature was listed in Table 2.2. The normal measurement process was to position the sample below the detection coils with the sample through the coils while measuring the output of the SQUID. The coils are wound in a second-derivative configuration in which the upper and lower single turns are counter wound with respect to the two-turn center coil. The magnetization of the sample was measured by moving the sample upward some distance and reading the voltage from the SQUID detector. The maximum field was applied about 7 T using NbTi coil. The resolution of magnet moment was better than 1×10^{-7} emu at 7 T.

Table 2.2: Specification of MPMS-7

Description	Specifications
Field range	± 7 T
Field stability	1 ppm/hour
Intrinsic field uniformity	0.01% (over 4 cm scan)
Field setting resolution	2×10^{-5} T ($0.0\le B\le0.6$ T) 2×10^{-4} T ($0.6\le B\le7.0$T)
DC magnetization -Differential sensitivity	1×10^{-8} emu ($0.0\le B\le1.0$ T) 1×10^{-7} emu ($1.0\le B\le2.0$ T) 1×10^{-6} emu ($2.0\le B\le7.0$ T)
-Absolute sensitivity	1×10^{-7} emu ($0.0\le B\le1.0$ T) 1×10^{-6} emu ($1.0\le B\le7.0$ T)
Temperature range	1.9 to 400 K

Temperature stability at the sample Space	< 0.05 K @ 300 K < 0.01 K @ 5.0 K
Temperature spatial variation in sample chamber	± 0.01 K over 8 cm ± 1.0 K over 15 cm @ 235 K

The measurement conditions are listed in Table 2.3. Although the magnetic field was a function of position due to the solenoid-type winding in the magnet, the variation of field was less than 0.05% for the scan length of 3 cm.

Table 2.3: Measurement condition for DC magnetization

Description	Specifications
Equipment	SQUID (Quantum Design MPMS-7)
Scan length	3 cm
Data points	32
Longitudinal	Iterative regression
Magnet charge mode	No overshoot

2. 4. 2 T_c measurements

The superconducting transition temperature (T_c) was determined from the temperature dependence of field cooled (FC) and zero field cooled (ZFC) DC magnetization measured with a SQUID magnetometer. The applied magnetic field was 1 mT with $H//c$. DC magnetization measurements were performed 10 s after reaching the target temperature, which was carried out with a temperature interval (ΔT) of 10 K between $10 \leq T \leq 80$ K and ΔT = 0.5 K between $80 \leq T \leq 110$ K. The scan length is set at 3 cm. Three data were averaged. Fig. 2.4 shows a typical example of a DC magnetization measurement to determine T_c in single crystal Nd-123 superconductor.

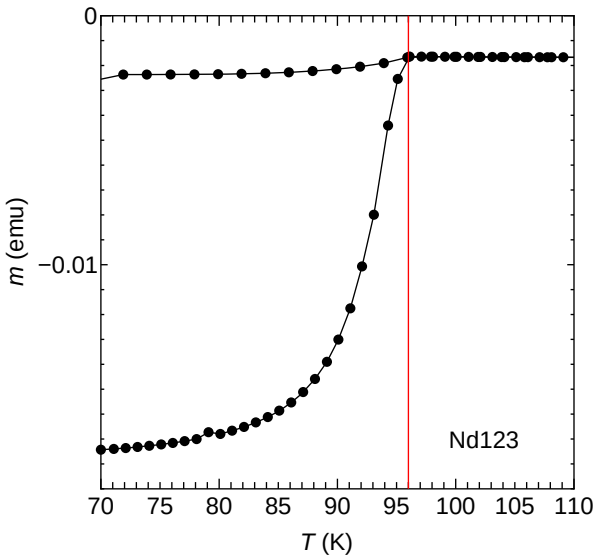

Fig. 2.4: DC magnetization measurement to determine T_c in single crystal Nd-123 superconductor.

2. 4. 3 Hysteresis measurements

Magnetization loops were measured using a DC magnetometer (SQUID). A large negative magnetic field (-7 T) was applied to ensure full penetration before starting a measurement. The magnetic field is applied with $\Delta\mu_0 H_a = 0.25$ T and $H /\!/ c$. The field is swept in no overshoot mode and persistent current mode. DC magnetization measurements were performed 10 s after reaching the target field. The scan length was 3 cm. Three data were averaged. Fig. 2.5 shows a typical example of hysteresis measurements in single crystal Nd-123 superconductor. The critical current density J_c is estimated from the measured magnetization hysteresis using the Bean model as

$$J_c = \frac{6a}{b(3a-b)}\Delta M, \qquad (2.1)$$

where ΔM is the magnetization width, a and b are the length and the width of the specimen, respectively.

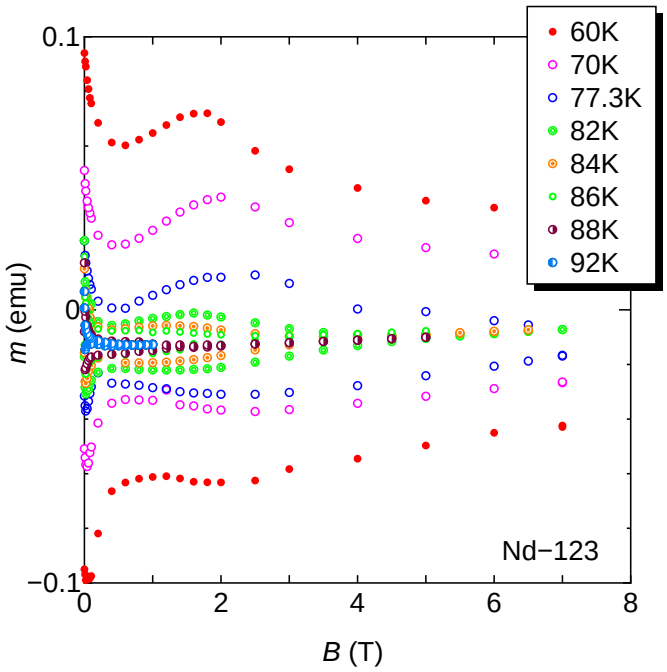

Fig. 2.5: A hysteresis measurements in single crystal Nd-123 superconductor.

2. 4. 4 Magnetic relaxation measurements

Magnetic relaxation was measured by monitoring the time decay of DC magnetization. A large negative magnetic field (-7 T) was applied to ensure full flux penetration before starting a measurement. The magnetic field was applied for *H*//*c*. The field was set in no overshoot mode and in persistent current mode. Magnetization measurements were performed immediately after reaching the target field. The scan length was 3 cm. Data were not averaged. Fig. 2.6 shows a typical example of relaxation measurement in Nd-123 superconductor. From the relaxation measurement, it is estimated *E*-*J* characteristics by using the following formulas:

$$J = \frac{12m}{w^2 d(3l - w)}, \tag{2.2}$$

$$E = -\frac{\mu_0}{2d(l + w)} \cdot \frac{\mathrm{d}m}{\mathrm{d}t}, \tag{2.3}$$

where m is the magnetization, l is the length, w is the width and d is the thickness of the specimen, E is the electric field and J is the current density, and the apparent pinning

potential U_0^* is estimated from the relaxation of current density by using the following formula:

$$-\frac{\mathrm{d}}{\mathrm{d}\log t}\left(\frac{J}{J_{\mathrm{c0}}}\right)=\frac{k_{\mathrm{B}}T}{U_0*}, \qquad (2.4)$$

where k_{B} is the Boltzmann constant, J_{c0} is the virtual critical current density in the creep free case, t is the relaxation time and T is the temperature.

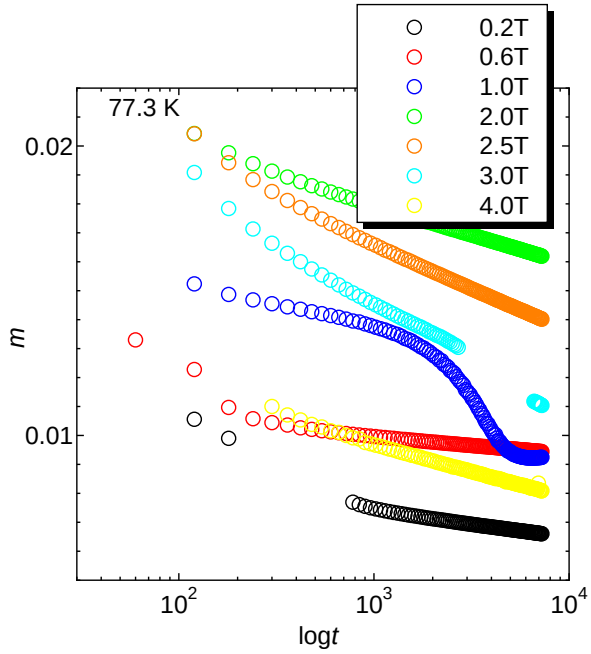

Fig. 2.6: A relaxation measurements in a single crystal Nd-123 superconductor.

References

1. Y. D. Tretyakov and E. A. Goodilin, *Pure Appl. Chem*. **76,** 1749, (2004)
2. Y. D. Tretyakov and E. A. Goodilin, *Russ. Chem. Rev*. **69**, 3, (2000)
3. J. M. S. Shakle, *Mater. Sci. Eng*. **R23**, 1 (1998)
4. Y. Shiohara and E. A. Goodilin, In *Handbook on the Physics and Chemistry of Rare-Earths*, K. A. Gschneidner, Jr., L. Eyring, M. B. Maple (Eds.), 67, *Elsevier*, Amsterdam (2000)
5. Y. D. Tretyakov and E. A. Goodilin, *Russ. J. Inorg. Chem*. **46**, S203, (2001)
6. E. A. Goodilin, N. N. Oleynikov, G. Yu. Popov, V. A. Shapanchenko, E. V. Antipov, G. V. Balakirev, Y. D. Tretyakov, *Physica C* **272**, 65 (1996)
7. E. Goodilin, M. Limonov, A. Panfilov, N. Khasanova, A. Oka, S. Tajima, Y. Shiohara, *Physica C* **300**, 250 (1998)
8. E. Goodilin, N. Khasanova, X. J. Wu, T. Kamiyama, F. Izumi, S. Tajima, Y. Shiohara, In *High Technology Subseries of the NATO Science Series*, **62**, G. Van Tendeloo, E. V. Antipov, S. N. putilin (Eds.) 145, Kluwer Academic, Dordrecht (1999)
9. E. A. Gudilin, I. A. Presnyakov, M. V. Tarasov, S. N. Mudretsova, A. F. Maiorova, J. Hester, N. N. Pleinikov, Y. D. Tretyakov, *Dokl. Chem*. **373**, 160, (2000)
10. E. Goodilin, A. Oka, J. G. Wen, Y. Shiohara, M. Kambara, T. Umeda, *Physica C* **299**, 279, (1998)
11. S. I. Yoo, N. Sakai, H. Takaichi, T. Higuchi and M. Murakami, *Appl. Phys. Lett.* **65**, 633 (1994)
12. M. Murakami, S. I. Yoo, T. Higuchi, N. Sakai, M. Watabiki, N. Koshizuka and S. Tanaka, *Physica C* **235-240** 2741 (1994)
13. H. Kojo, S. I. Yoo, N. Sakai and M. Murakami, *Superlattices Microstruct.* **21**, 37 (1997)
14. K. Sawada, S. I. Yoo, N. Sakai, T. Higuchi and M. Murakami, *Proc. 4th Euro Ceramics* **vol. 6** (Faenza: Gruppo Editoriale Faenza Editrice S. p. A.)293-298 (1995)
15. M. Muralidhar, M. Jirsa, N. Sakai and M. Murakami, *Appl. Phys. Lett.* **79**, 3107 (2001)

Chapter 3 Flux pinning property in a single crystal $NdBa_2Cu_3O_y$ superconductor

3. 1 Introduction

Among high-temperature superconductors, $REBa_2Cu_3O_y$ (RE denotes a rare earth element, RE-123) is one of the most interesting materials to study, as it is considered to be a strong candidate for practical applications. In particular, RE-123 with RE = Nd and Sm fabricated under a low oxygen partial pressure exhibits high T_c and large J_c values [1, 2] than Y-123 superconductors. In RE-Ba-Cu-O system, there is a wide range of composition in the RE-Ba solid solution. The chemical composition of RE-Ba-Cu-O system can be described as $RE_{1+x}Ba_{2-x}Cu_3O_{7-\delta}$. When RE-Ba-Cu-O is synthesized in a reduced oxygen atmosphere, x shifts to lower values, which means that the chemical composition close to 123 stoichiometry, and thereby T_c is remarkly improved. Even in such a class, there exists a slight chemical variation and thus RE substituted Ba regions of low-T_c phase are distributed in the high-T_c matrix. These substituted regions are also effective in pinning. In RE-123 single crystal, an anomalous J_c enhancement with field, which is so called “fishtail” or “peak effect”, is commonly observed. In single crystal RE-123 superconductors, it has been reported that the critical current density J_c has a broad peak due to the pinning of a low T_c phase in which RE sites are substituted by Ba [3, 4].

The flux creep-flow model is useful for an investigation of the pinning property and the corresponding behavior of flux lines, such as the number of flux lines in the flux bundle, g^2 [5]. In this model, another important parameters used for the characteristics as well as g^2 are the most probable value of pinning strength (A_m) and a parameter representing the distribution width of pinning strength (σ^2). The detailed explanation of the model and these parameters is given in Appendices. For further details of the numerical calculation, see [6].

In this chapter, the relation between the apparent pinning potential U_0^* and the critical current density J_c is investigated to find out the mechanism of the peak effect in a single crystal $NdBa_2Cu_3O_y$ superconductor. The purpose of this research work in the investigation of the flux pinning mechanism in NEG-123 bulk superconductor. However, the pinning mechanism in this system is very complicated because of additional pinning by 211 particles and other defects such as nano-lamellas. Hence, Nd-123 single crystal

is used in this chapter to find out the mechanism of the peak effect and those discussions help to explain the peak effect of NEG-123 bulk superconductor.

3. 2 Experimental

Specimen was a flux-grown $NdBa_2Cu_3O_y$ single crystal superconductor. The sample dimension was $1.60\times1.45\times0.65$ mm^3 and the critical temperature T_c was 96.0 K, which was determined by temperature dependence of zero-field-cooled (ZFC) and field-cooled (FC) magnetization by a Quantum Design SQUID magnetometer. The magnetization in a magnetic field along the *c*-axis was measured at different temperatures. The critical current density J_c was estimated from a measured magnetization hysteresis using the Bean model. The irreversibility field was determined by the field at which J_c was reduced to 1×10^6 A/m^2. The *E-J* characteristic was estimated from a relaxation of magnetization over a range of electric field from 10^{-12} to 10^{-8} V/m and also the apparent pinning potential U_0^* is estimated from a relaxation of magnetization.

3. 3 Results and discussion

In Fig. 3.1, the observed magnetic field dependence of the critical current density J_c is shown in the temperature region of 50-94 K.

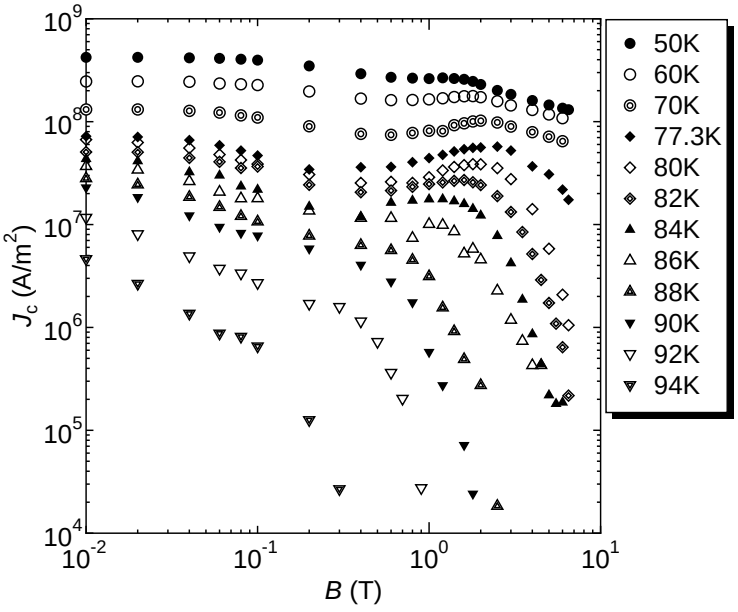

Fig. 3.1: Magnetic field dependence J_c at various temperatures.

The broad peak was observed in the temperature region of 60-88 K. The observed

irreversibility field B_i, peak field B_p and dip field B_d at which J_c takes a minimum value are shown in Fig. 3.2. It is found that the field B_d is almost constant with temperature, while the peak field B_p increases with temperature, takes a maximum at 77.3 K, and then, decreases with increasing temperature. B_d and B_p disappear above 80 K due to the flux creep. If the peak effect originated from the field-induced pinning mechanism, B_d would decrease monotonically with increasing temperature reaching zero at T_c of the low T_c phase as shown by the dot line.

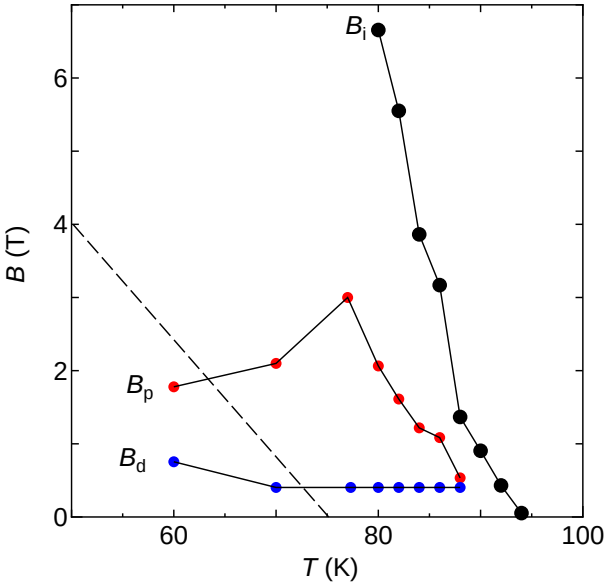

Fig. 3.2: Temperature dependence of peak field (B_p), dip field (B_d) and irreversibility field (B_i).

In previous measurements, Matsushita *et al.* [7] described the temperature dependence of the peak field (B_p) and the dip field (B_d) at which J_c takes on a minimum value and the irreversibility field (B_i) for specimen Y-123 with addition 211 particles as shown in Fig. 3.3. The temperature dependence of these characteristics fields are similar to each other, suggesting that a temperature scaling of the pinning force density holds approximately, if the magnetic field is normalized by B_i. This result also indicates that the peak effect does not directly originate from a field-induced pinning mechanism.

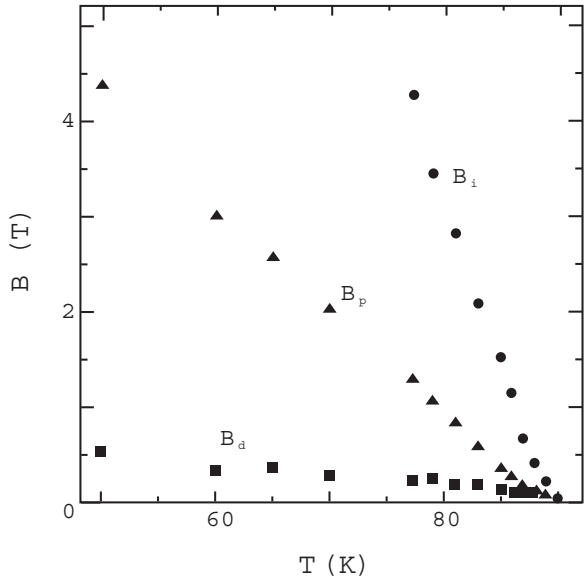

Fig. 3.3: Peak field (B_p), dip field (B_d) and irreversibility field (B_i) in specimen of Y-123 with addition of 211 phase particles. This is Fig. 4 of ref. [7].

The apparent pinning potential U_0^* is estimated from the relaxation of magnetization, which is shown in Fig. 3.4.

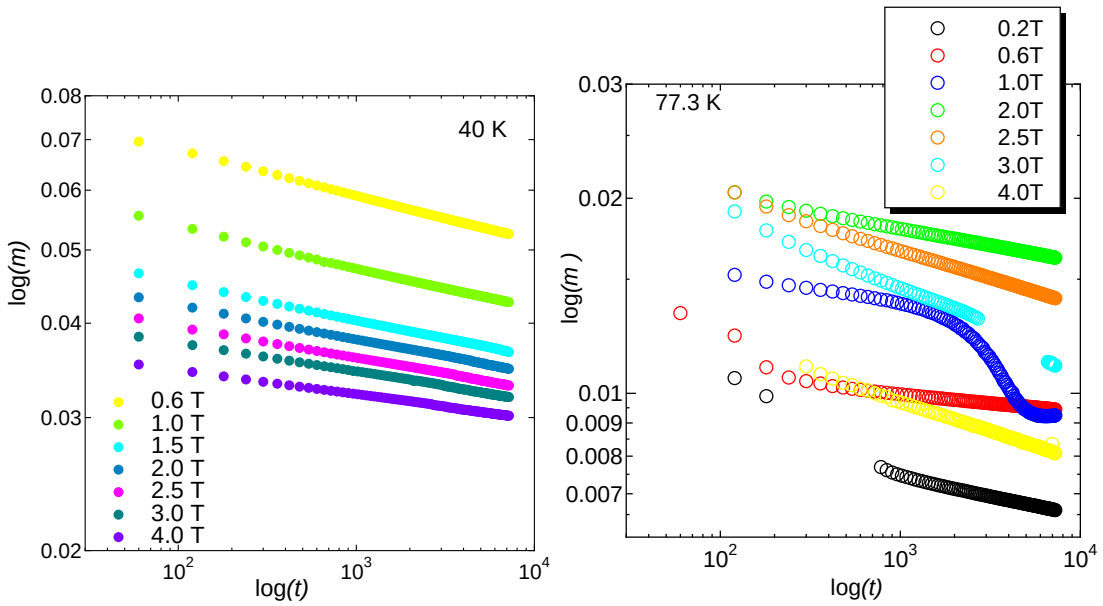

(a) (b)

Fig. 3.4: Magnetic relaxation in Nd-123 single crystal superconductor at (a) 40 K and (b) 77.3 K

In Fig. 3.5(a), experimental results of field dependences of the apparent pinning potential U_0^* and the critical current density J_c at 40 K, where the peak effect is not observed, are shown. In this case, U_0^* increases with magnetic field in spite of a monotonous decrease of J_c.

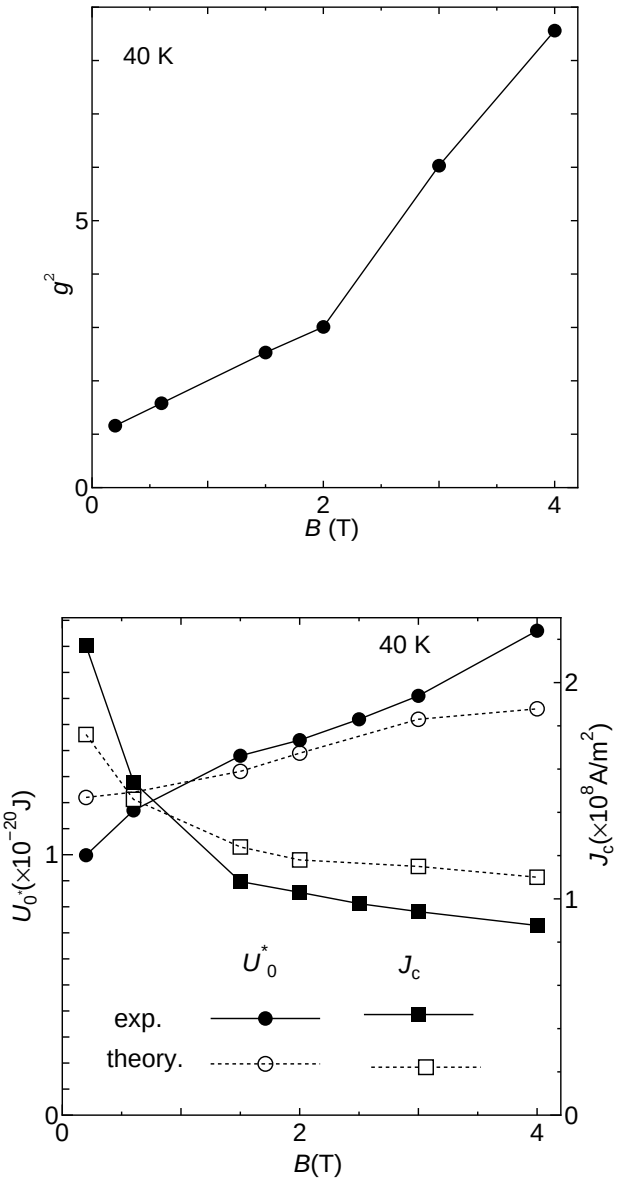

Fig. 3.5: (a) Magnetic field dependence of U_0^* and J_c at 40 K; (b) Magnetic field dependence of g^2 at 40 K.

These results are compared with the theoretical prediction of the flux creep-flow model. The theoretical results of U_0^* and J_c are also shown in Fig. 3.5(a). The parameters used in the theoretical calculation are: $A_m = 9.73 \times 10^8$, $\sigma^2 = 0.01$, $\gamma = 0.87$, $m = 2.05$ and $\delta = 2.0$, and g^2 is used as a fitting parameter. It is found that g^2 increases with increasing magnetic field, as shown in Fig. 3.5(b). It is found that the agreement is good between theoretical and experimental results. The monotonous decrease of J_c is simply explained by a monotonous decrease of J_{c0} as in Eq. (39) of Appenedix-1 (flux creep-flow model).

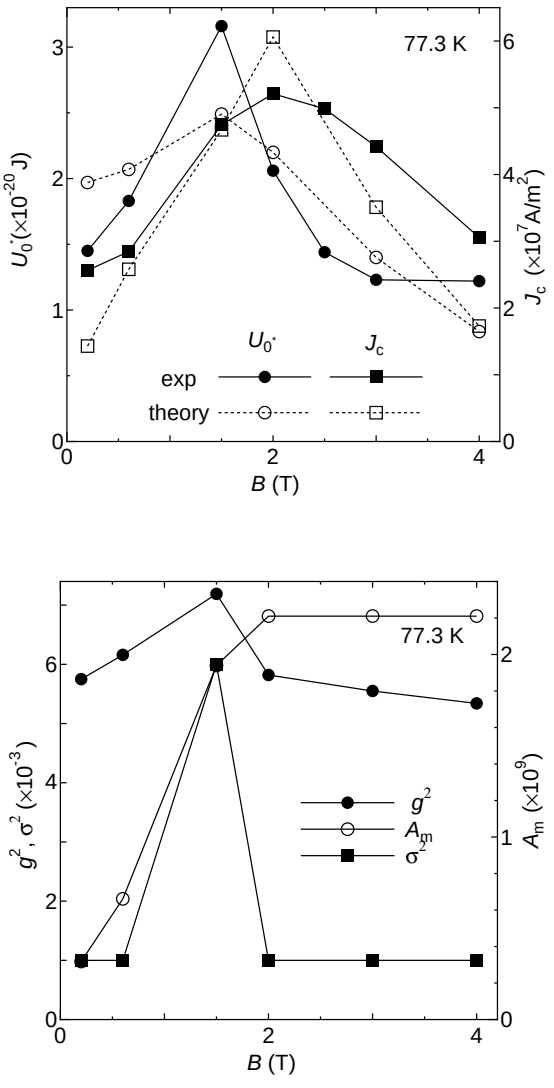

Fig. 3.6: (a) Magnetic field dependence of U_0^* and J_c at 77.3 K; (b) Magnetic Field dependence of A_m, g^2 and σ^2 at 77.3 K

Fig. 3.6(a) shows the results at 77.3 K where the peak effect is observed. U_0^* and J_c increase with magnetic field in the magnetic field range of 0.2-1.5 T. However, U_0^* decreases in spite of further increase of J_c in the field range of 1.5-2.0 T. Magnetic field dependence of parameters A_m, g^2 and σ^2 obtained so as to get a good agreement are shown in Fig. 3.6(b). The other parameters used in this theoretical calculations are: γ=0.85, m=2.05 and δ=2.0. A_m and g^2 increase up to 1.5 T with increasing magnetic field, and then g^2 decreases, in spite of increase of A_m up to 2.0 T, and from 2.0 T, A_m is constant. At 1.5 T, σ^2 has a maximum value.

The enhancement of A_m is directly related to the enhancement of J_c, and hence, can be explained by the both mechanisms. Above 2 T, A_m is constant and this is consistent with the decrease of J_c. The change of σ^2 can also be explained by the both mechanisms. In the field region of $B < B_d$, σ^2 is expected to be small, as the distribution of the flux pinning strength has a sharp peak around a small value. In the field region of $B > B_p$, the similar thing takes place around a strong pinning force, resulting in a small σ^2 again. In the intermediate region, weakly pinning regions and strongly pinning regions coexist, resulting in a large σ^2. Hence, the behavior of g^2 is important to specify the correct mechanism.

In the field region of 0.2-1.5 T, g^2 increases with increasing magnetic field. This is consistent with the behavior at 40 K. However, g^2 decreases with increasing magnetic field for 1.5-2.0 T. It is not possible to explain the reduction of g^2 by the field-induced pinning mechanism. The reduction of g^2 means the reduction of C_{66}, i.e., the softening of flux lines. This results show that the disorder transition occurs in the field ranges between B_d and B_p.

The observed results are approximately consistent with the theoretical predictions of Brandt *et al*. [8] model of the order-disorder transition that the Lindemann criterion does define the condition for proliferation of dislocations in the flux lines lattice at the order-disorder transition by the reduction of transverse flux bundle size. Such the reduction of transverse flux bundle size is correlated with the reduction of the number of flux lines in the flux bundle, g^2, which is consistent with our observed results.

3. 4 Summary

To investigate the pinning mechanism of the peak effect of a single crystal $NdBa_2Cu_3O_y$ superconductor, the behavior of pinning parameters were investigated. The following results are obtained:

1. At 40 K, where the peak effect is not observed, the monotonous decrease of J_c is simply explained by a monotonous decrease of J_{c0} as in Eq. (3.2). At 77.3 K, the enhancement of A_m is directly related to the enhancement of J_c, and hence, can be explained by the both mechanisms. The peak of σ^2 is also explained by the two mechanisms. The reduction of g^2 can be explained only by the softening of flux lines, which is considered to be caused by the disorder transition of flux lines.
2. The field-induced pinning mechanism does not explain the temperature dependences of the peak field B_p and the dip field B_d.
3. From the above reasons, it is concluded that the peak effect originates from the disorder transition of flux lines.

References

1. S. I. Yoo, N. Sakai, T. Takaichi, T. Higuchi and M. Murakami, *Appl. Phys. Lett.* **65**, 633 (1994).
2. M. Murakami, S. I. Yoo, T. Higuchi, N. Sakai, M. Watahiki, N. Koshizuka and S. Tanaka, *Physica C* **235-240**, 278 (1994).
3. M. Daumling, M. J. Seuntjens and D. C. Larbalestier, *Nature* **346**, 332 (1990).
4. H. Suematsu, H. Okamura, S. Lee, N. Nagaya and H. Yamauchi, *Physica C* **338**, 96 (2000).
5. T. Matsushita, T. Tohdoh and N. Ihara, *Physica C* **259**, 321 (1996).
6. M. Kiuchi, K. Noguchi, T. Matsushita, T. Kaito, T. Hikata and K. Sato, *Physica C* **278**, 62 (1997).
7. T. Matsushita, D. Yoshimi, M. Migita and E. S. Otabe, *Supercond. Sci. Technol*. **14** 732 (2001)
8. E. H. Brandt and G. P. Mikitik, *Supercond. Sci. Technol*. **14**, 651, (2001).

Chapter 4 Flux pinning properties of (Nd, Eu, Gd)$Ba_2Cu_3O_y$ (NEG-123) superconductor with 211 phase particles

4. 1 Introduction

The pinning mechanism of the irreversibility field and that of the peak effect are different in Y-123 or Nd-123 [1, 2]. In fact J_{cp} is likely to decrease while B_i tends to increase by addition of 211 or 422 phase in these superconductors. That is, B_i determined from the attractive pinning by 211 phase particles which is dominant at high magnetic fields, and J_{cp} is determined from the repulsive pinning interactions by oxygen deficient regions or substituted regions. Superior performance has been reported for higher peak critical current density J_{cp} and irreversibility field B_i in (Nd, Eu, Gd)-123 (NEG-123) bulk superconductors at 77.3 K as compared to Y-123 or Nd-123 [3-6].

Muralidhar *et al*. [7, 8, 9] investigated the properties of J_{cp} and B_i at 77.3 K in $Nd_{0.33}Eu_{0.33}Gd_{0.33}Ba_2Cu_3O_y$ superconductors with addition of various 211 phases. The behaviors of J_{cp} and B_i with addition of 211 phase in this superconductors are described in Chap. 1 and are complicated.

In order to understand the change in J_c-B characteristics, they performed chemical analyses through microstructural observation and found a change in the chemical composition of a NEG-123 specimen with 211 phase addition, which might affect the J_{cp} and B_i. They speculated [7] that such peak effect was ascribed to the field-induced pinning by RE-rich clusters dispersed in NEG-123 systems with 211 particles addition, and that such field-induced pinning was active in parallel with the pinning by 211 particles. On the other hand, they observed a pronounced peak effect with J_{cp} of 7×10^8 A/m^2 (peak at B = 4.5 T) and high B_i over 14 T which described in chapter 1. [10], and found new pinning centers, i.e., nanoscale lamellae structure of NEG/Ba-rich clusters and proposed that such new structures played the significant role for the increase in B_i. Muralidhar *et al*. [10, 11, 12] investigated also the microstructure by STM and DFM image for $Nd_{0.33}Eu_{0.38}Gd_{0.28}Ba_2Cu_3O_y$ with addition of 3, 5, 7, 10 and 40 mol% NEG-211 phase, which revealed that a new defects, i.e., the nano-lamella structure systematically appeared in samples with 3-10 mol% of NEG-211 phase and these nano-lamella structure was absent in the one with 40 mol% NEG-211 phase. From the STM analysis they found that the average spacing of the nano-lamella structure was around 3-4 nm (3 mol%) and again increased with increasing 211 phase, i.e., the change of nano-lamella structure was observed by addition of 211 phase. It was found [3, 11, 12] that the pinning performance could be tailored in NEG-123 by controlling chemical

ratio of Nd, Eu and Gd elements together with addition of 211 phase. In previous measurements, however, a clear evidence was not given for the above speculation on the pinning centers and corresponding mechanisms responsible for the increase in J_{cp} and the decreases in B_i with 211 phase addition to NEG-123 materials. For further improvement of J_{cp} and B_i, such kind of explanation is very important.

Therefore, in the present study, we focus on the most promising $Nd_{0.33}Eu_{0.38}Gd_{0.28}Ba_2Cu_3O_y$ superconductor which shows a high performance at high fields and study the variations of J_{cp} and B_i with the volume fraction of 211 phase to find out the mechanisms which determine the peak effect and B_i. Then, a discussion is given on the possible defects and the corresponding pinning mechanism which can explain the experimental results.

4. 2 Experimental

Specimens were prepared by ISTEC group. The details of the specimen preparation is described in section 2.3.2. The size and dispersion of 211 phase in the 123 matrix depends on the initially added 211 size. In the present case, 75 nm sized 211 phase particles were used before melt processing and one can expect that the final size of 211 particles between the 100 to 500 nm, which was already confirmed by TEM analysis and also by high angle dark field scanning transmission electron microscopy with atomic resolution [13].

The magnetization in a magnetic field along the *c*-axis was measured using the Quantum Design SQUID magnetometer. The onset superconducting transition temperature of all the samples was in the range of 92.5-93.3 K. The magnetization critical current density J_c was measured and the irreversibility field was determined by the field at which J_c was reduced to 1×10^6 A/m^2. The measurements were carried out in the magnetic field range of 0.01-7 T and in the temperature range of 77.3-80 K. The upper critical field B_{c2} is measured from the field-cooled (FC) and zero field-cooled (ZFC) DC magnetization measurements in the magnetic field range of 0.5-7 T and in the temperature range of 70-100 K.

4. 3 Results and discussion

In Fig. 4.1(a) and (b), the magnetic field dependence of J_c with different volume fractions of NEG-211 and EG-211 phases at 80 K is shown, respectively. A pronounced increase in J_c at peak field region occurs by increasing the volume fraction of both NEG-211 and EG-211 phases. On the other hand, the J_c at high fields is deteriorated

with addition of 211 phase suggesting a decrease in B_i. The dependence of J_{cp} and B_i on the volume fractions of 211 phase are shown in Fig. 4.2. Figure 4.3 shows the dependence of J_{cp} on the volume fractions of 211 phase at 77.3 K. The highest value of J_{cp} obtained for the specimen with 10 mol% NEG-211 reached almost 6×10^8 A/m^2. At this temperature the irreversibility field exceeded 7 T and was too high to measure. It is found from Fig. 4.2 that J_{cp} increases with increasing volume fraction of EG-211 phase. A similar dependence is obtained also for the addition of NEG-211 phase, although J_{cp} is minimum at 7 mol% of NEG-211 phase. The same behavior is observed at 77.3 K as shown in Fig. 4.3. On the other hand, B_i decreases with increasing volume fractions of EG-211 phase. The similar dependence is found also for addition of NEG-211 phase, although B_i is maximum and reaches 7 T even at 80 K at 7 mol% of NEG-211 phase. From the change in J_{cp} and B_i with addition of 211 phases, it is found that there is no large difference in the effect of addition between EG-211 and NEG-211 phases. Such variations with addition of 211 phases are completely opposite to the cases of Y-123 and Nd-123.

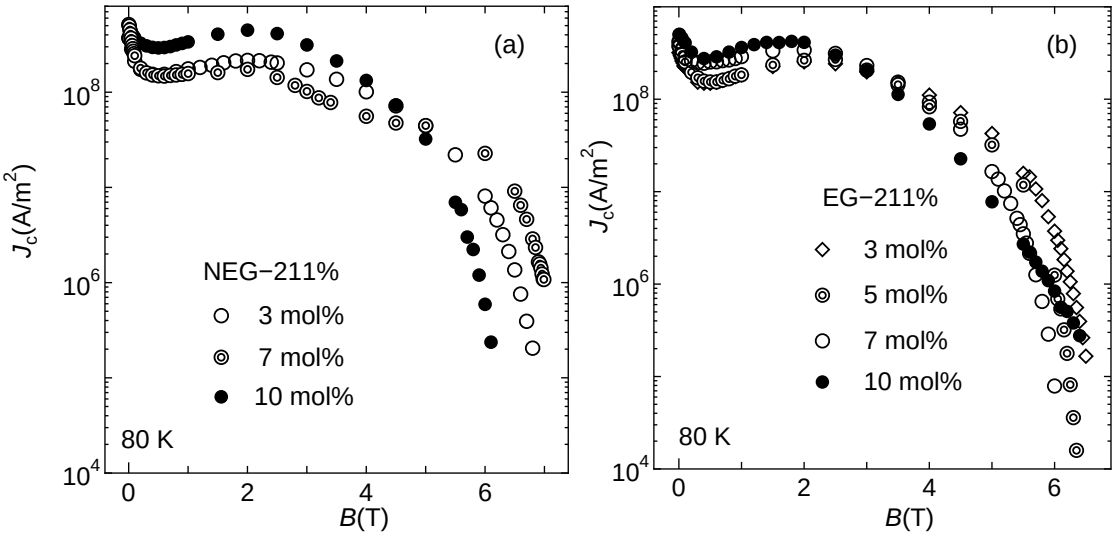

Fig. 4.1: Field dependence critical current density J_c in NEG-123 system with different volume fraction of (a) NEG-211 and (b) EG-211 particles at 80 K.

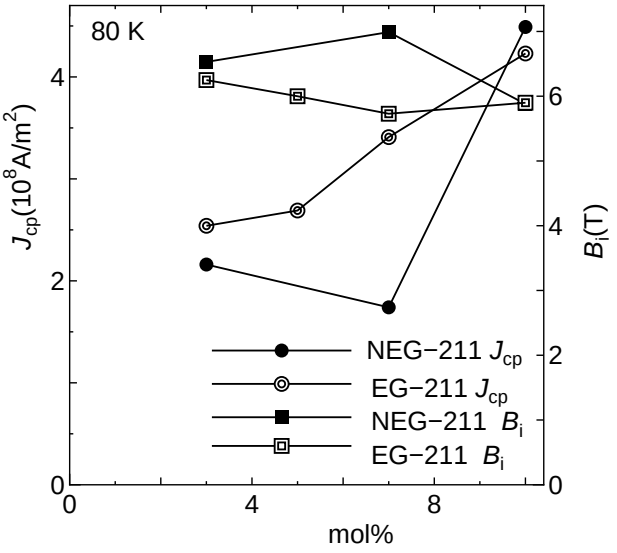

Fig. 4.2: Variation of the peak critical current density J_{cp} and irreversibility field B_i with different volume fraction of 211 particles at 80 K.

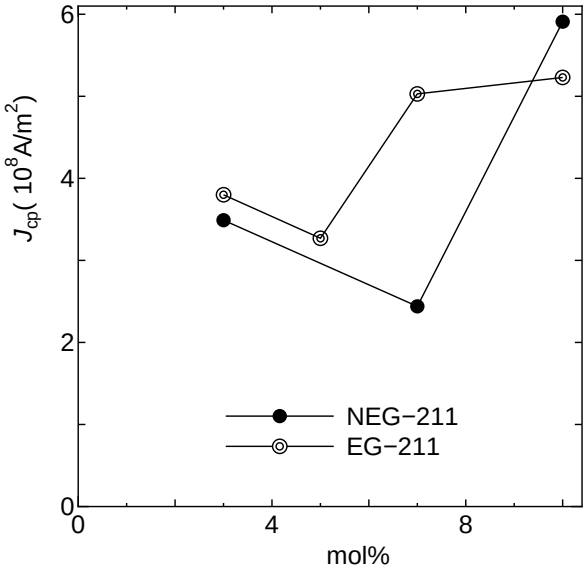

Fig. 4.3: Variation of the peak critical current density J_{cp} with different volume fraction of 211 particles at 77.3 K.

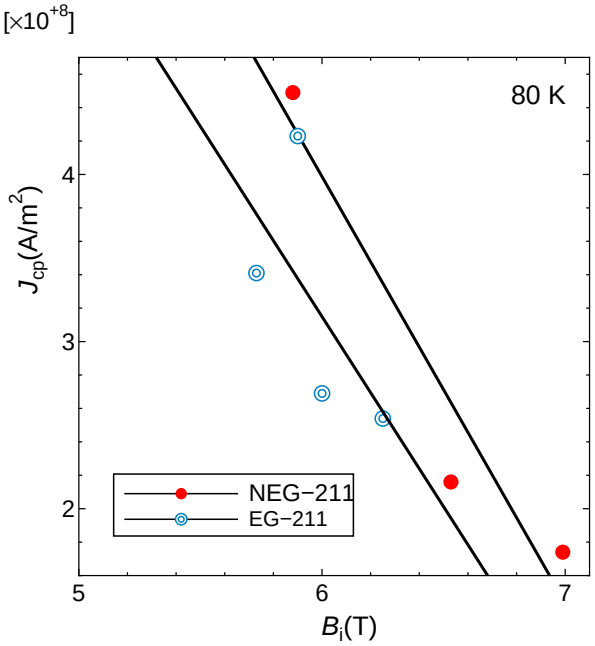

Fig. 4.4: A negative correlation between peak critical current density J_{cp} and irreversibility field B_i in NEG-123 system.

However, it can be said from the above results that there exists a negative correlation between J_{cp} and B_i as shown in Fig. 4.4. This strongly suggests that the pinning mechanisms which determine J_{cp} and B_i are different. The exceptional behavior of the specimen of 7 mol% of NEG-211 might be caused by particular chemical composition of dispersed 211 phase than the nominal chemical composition.

In order to explain responsible pinning centers and corresponding pinning mechanisms for the new behavior of J_{cp} and B_i, a discussion is necessary, which is as follows:

Substituted regions/oxygen deficient regions which exist naturally are known to cause the peak effect in Nd-123 and Y-123. In the present measurements, however, the peak effect became pronounced by increasing the volume fractions of 211 phases, whereas substituted regions or oxygen deficient regions are not controlled. Hence, these defects are considered not to be responsible for the increase in J_{cp}.

Murakami *et al* [14] showed that that J_c is proportional to V_f/d as theoretically predicted, where V_f is the volume fraction of Y211 particles and d is the diameter of Y211 (Fig. 4.5) [15].

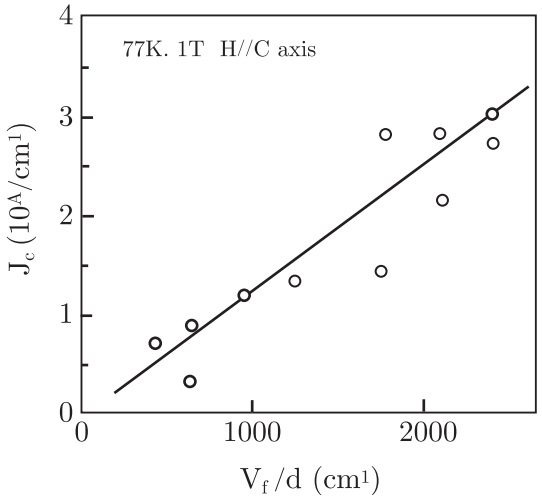

Fig. 4.5: Plots of J_c (77 K, 1 T with $H \parallel c$-axis) against V_f/d (211) for various melt-processed Y-Ba-Cu-O samples [14].

It is known that 211 particles act as strong pinning centers. In fact the critical current density of about 3×10^8 A/m^2 can be expected at 1 T for the specimen with 10 mol% 211 particles (average size, d = 250 nm) from the relationship between J_c and surface area of 211 phase particles from the result in Fig. 4.5. However, this will be reduced to about 2×10^8 A/m^2 at 2.5 T, and hence, the observed critical current density of about 6×10^8 A/m^2 at the peak field can not be explained by the mechanism of 211 phase particles. In addition, the pinning mechanism of normal 211 particles is the condensation energy interaction with the pinning force which decreases monotonically with increasing magnetic field. Hence, the pinning by 211 particles does not directly play the role in increasing J_{cp}.

Another possibility of the peak effect by 211 particles is the order-disorder transition of the flux lines, i.e., a transitional change of flux lines from the ordered state with a low J_c to the disordered state with a high J_c. The enhancement of the pinning efficiency at the peak effect is considered to be caused by the softening of elasticity of flux lines. In chapter 3, it was shown that the peak effect in a single crystal $NdBa_2Cu_3O_y$ superconductor is caused by the order-disorder transition of flux lines under the flux pinning by substituted regions with lower-T_c. For occurrence of the order-disorder transition, however, the pinning centers should be sufficiently small that an appropriate variation in the pinning efficiency could be realized by a slight deformation of flux lines. This requires a pinning potential quickly varying in space. On the other hand, the size of

211 particles is much larger than the flux line spacing. Hence, the 211 particles do not seem to contribute to the peak effect also from a softening of flux lines for the disorder transition.

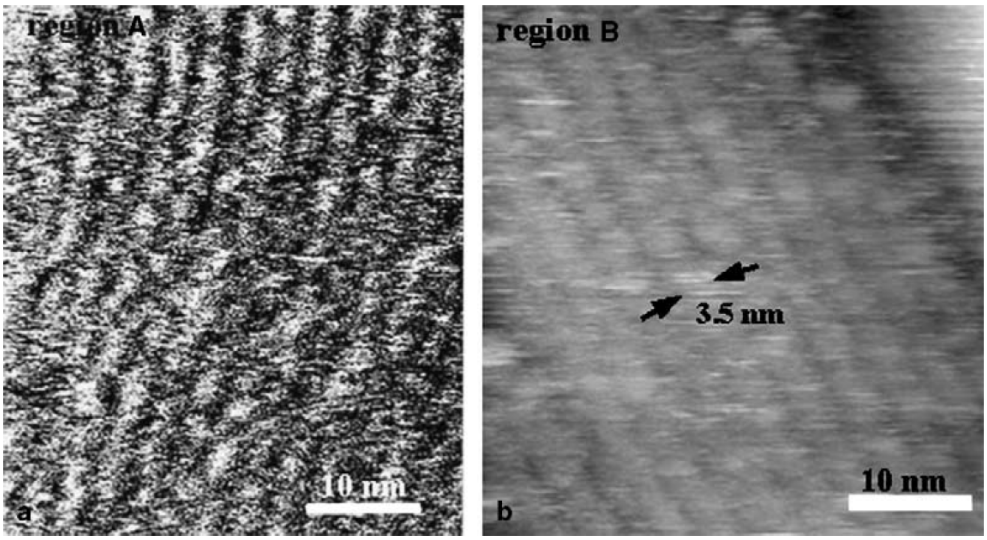

Fig. 4.6: High magnification STM image of the cleaved surface of ($Nd_{0.33}Eu_{0.38}Gd_{0.28}Ba_2Cu_3O_y$) sample. Note that the formation of an island structure of nano-lamellas with the average period of about 3.5 nm. This is Fig. 3 of ref. 13.

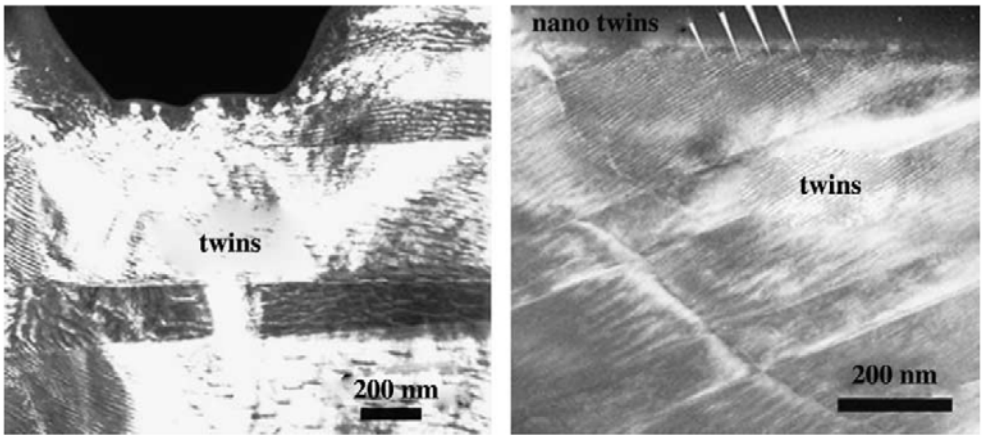

Fig. 4.7: TEM micrograph of a ($Nd_{0.33}Eu_{0.38}Gd_{0.28}Ba_2Cu_3O_y$) sample with 5 mol% NEG-211. Note the nanoscopic twin-like fine structure deformed in a zigzag manner (left figure); TEM micrograph of the same material with 10 mol% NEG-211 (right figure). This is Fig. 1 of ref. 13.

Another candidate for the pinning centers responsible for the peak effect is nano-lamellas. These defects are considered to be in the normal state, since the superconductivity in high-temperatures is quite sensitive to the chemical composition. In fact, superconductivity has not been reported in single phase specimens with such a NEG-rich chemical composition. Thus the pinning mechanism of nano-lamellas can not be the field-induced one but the usual condensation energy interaction, the strength of which decreases monotonically with increasing field. The observed peak effect can be explained only by the order-disorder transition of flux line with the pinning by nano-lamella structures. This seems to be possible, since their size is sufficiently small (in Figs. 4.6 and 4.7, it is shown that the average size of nano-lamella strucrures is about 3.5 nm) that those can provide a sharp variation in the flux pinning strength by a slight rearrangement of flux lines. It should be noted that any kind of pinning centers or pinning mechanisms can contribute to the order-disorder transition. That is, the corresponding pinning centers are substituted regions or oxygen deficiencies in Nd-123 and Y-123 with repulsive pinning (kinetic energy interaction) and nano-lamella structures in the present system with attractive pinning (condensation energy interaction). But the important point is that the size of pinning centers should be sufficiently small.

The decrease in B_i with increasing volume fraction of 211 phase is incompatible with the flux pinning by 211 particles themselves. One possible explanation may be a deterioration of the Bose-glass state of flux lines. That is, the high irreversibility field attained by the stabilization of flux lines in the Bose-glass state by the *c*-axis correlated nano-lamellas [16] seems to be degraded by the disturbance by 211 particles. However, the enhancement of the peak critical current density by the 211 particles addition suggests a rather stronger stabilization of the Bose-glass state by the addition, resulting in contradiction with experiments, if the scenario of the stabilization of the Bose-glass state is believed. In addition, such an enhancement of the pinning strength can be simply explained by the correlated pinning independently of the Bose-glass state.

Since the pinning interaction of 211 particles is not so weak, there should exist some contribution to the irreversibility field from 211 particles. Hence, the degradation in the irreversibility field can only be attributed to deterioration of some superconducting property. Such a deterioration seems to be caused by the proximity effect as in the substituted regions in Nd-123 [17]. In the present specimens, since the number density of nano-lamella structures is very high, the proximity effect between thin superconducting region and layered nano-lamella structures seems to be significant, resulting in deterioration of the superconducting property such as B_{c2} in the

superconducting matrix. This explains the decrease in B_i through the decrease in the upper critical field, when the fraction of the added 211 phase is high.

To clarify such degradation of B_i through the decrease in the upper critical field B_{c2}, we estimated the upper critical field B_{c2} of all specimens at 80 K. In Fig. 4.8, temperature dependence of upper critical field B_{c2} in NEG-123 system with different volume fraction of (a) NEG-211 and (b) EG-211 particles are determined. Then by extrapolating those experimental data by theoretical calculation we determined B_{c2} at 80 K.

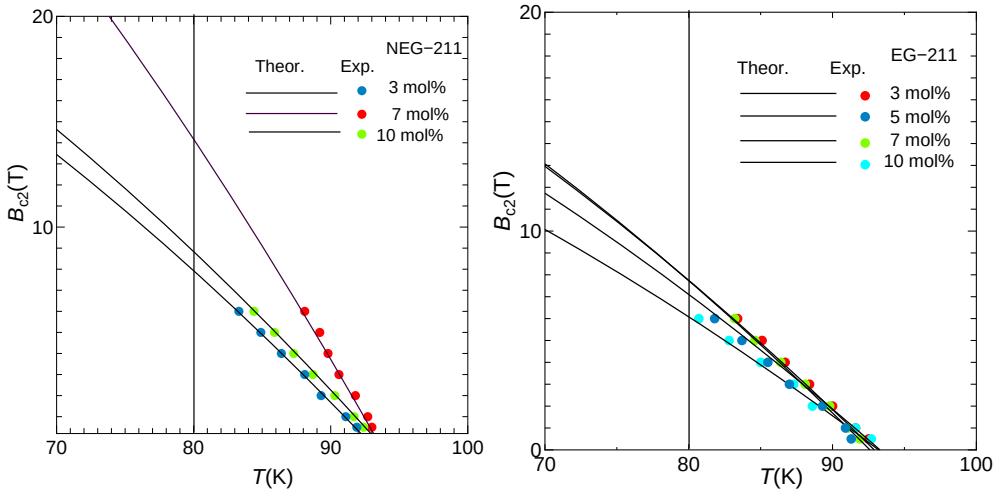

Fig. 4.8: Temperature dependence of upper critical field B_{c2} in NEG-123 system with different volume fraction of (a) NEG-211 and (b) EG-211 particles.

It is speculated that the degradation of B_i comes from the degradation of the superconducting property, i.e., the degradation of either critical temperature T_c or upper critical field B_{c2}. Fig. 4.9 (a) shows the variation of T_c with 211 phase particles and it is found that T_c is almost constant with increasing volume fraction of 211 phase particles. Hence, it is considered that the degradation of B_i does not come from the property of T_c. On the other hand, the degradation of upper critical field B_{c2} at 80 K with increasing the volume fraction of 211 phase particles is found in Fig. 4.9 (b).

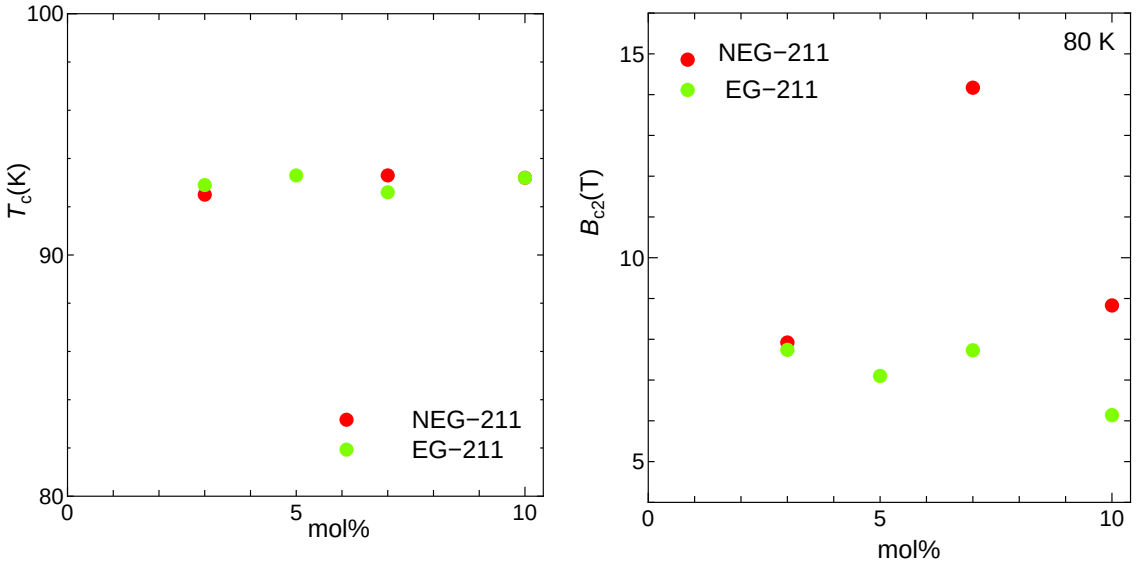

Fig. 4.9: (a) Variation of critical temperature T_c with 211 phase particles and (b) Variation of upper critical field B_{c2} with 211 phase particles at 80 K.

Then, in Fig. 4.10, it is shown that the relationship between the irreversibility field B_i and the upper critical field B_{c2} at 80 K. It is found a strong correlation between B_i and B_{c2} and it suggests that the degradation of B_i comes from the degradation of B_{c2} by the proximity effect.

On the other hand, the experimental results of critical current density J_c at 80 K are compared with the theoretical prediction of the flux creep-flow model (flux creep-flow model described in Appendix-1). The theoretical results of J_c are also shown in Fig. 4.11. The parameter and the estimated upper critical field B_{c2} used in the theoretical calculation are shown in the table 4.1. The pinning parameters A_m, m, γ, δ, σ^2 and the number of flux lines in the flux bundle, g^2, are determined so that a good fit between theoretical and experimental results and it is found that the agreement is good at the low and high field region. The enhancement of J_c with increasing 211 phase particles at low field region can be explained by the enhancement of A_m. But the exceptional 7 mol% of NEG-211 specimen has smaller A_m value due to lower J_c. On the other hand, the distribution width of pinning strength σ^2 value are 0.01-0.014.

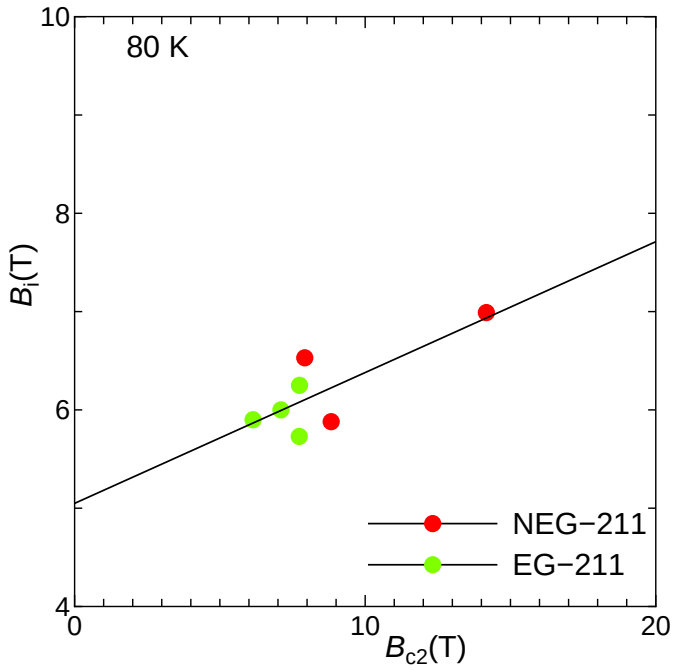

Fig. 4.10: Relationship between upper critical field B_{c2} and irreversibility field B_i at 80 K.

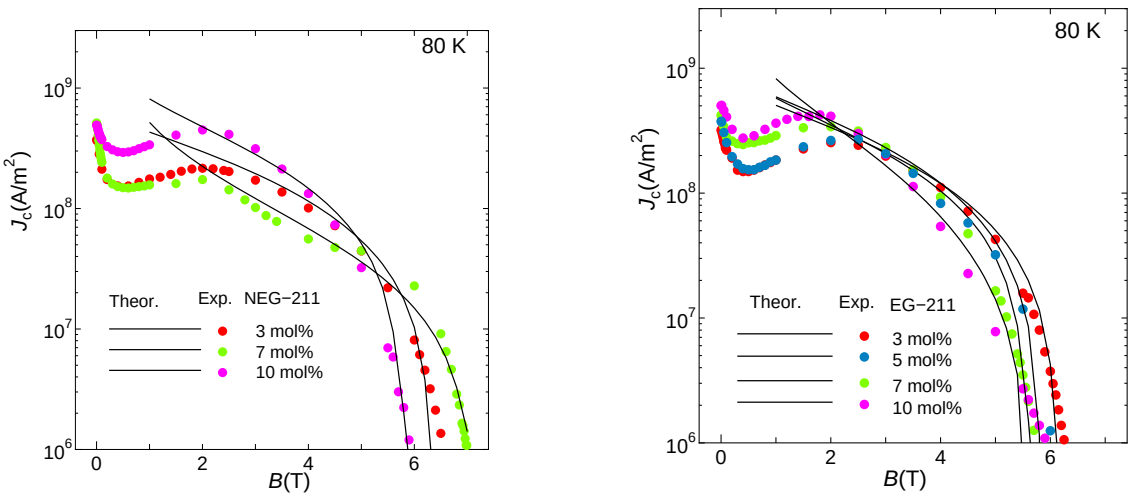

Fig. 4.11: Theoretical fitting of J_c-B curve with experimental results by using flux creep-flow model at 80 K.

But the 10 mol% of EG-211 has large σ^2 as the critical current density J_c of this

specimen has exceptional shape in the high field region compared with other specimens. Then a comparison of the irreversibility field between theoretical and experimental results is observed to clarify the theoretical result which is shown in Fig. 4.12. These results also suggest that the agreement is good between theoretical and experimental results

Table 4.1: Upper critical field B_{c2} at 80 K, B_{c2} (0), critical temperature T_c and pinning parameters used for theoretical calculation.

Specimen	T_c	B_{c2} **(80 K)**	B_{c2} **(0)**	A_m	σ^2	γ	m	g^2
NEG-211 (3) mol%	**92.5**	**7.92**	**31.46**	**5.8e10**	**0.014**	**0.98**	**2**	**6.40**
NEG-211 (7) mol%	**93.3**	**14.17**	**53.52**	**4.2e10**	**0.01**	**0.1**	**2**	**6.58**
NEG-211(10) mol%	**93.2**	**8.83**	**33.57**	**7.8e10**	**0.01**	**0.73**	**2**	**3.70**
EG-211 (3) mol%	**92.9**	**7.74**	**29.98**	**5.0e10**	**0.01**	**0.94**	**2**	**6.4**
EG-211 (5) mol%	**93.3**	**7.10**	**26.84**	**6.6e10**	**0.012**	**0.95**	**2**	**6.22**
EG-211 (7) mol%	**92.6**	**7.73**	**30.50**	**7.0e10**	**0.012**	**0.84**	**2**	**4.6**
EG-211 (10) mol%	**93.2**	**6.14**	**23.11**	**5.5e11**	**0.055**	**0.50**	**2**	**9.5**

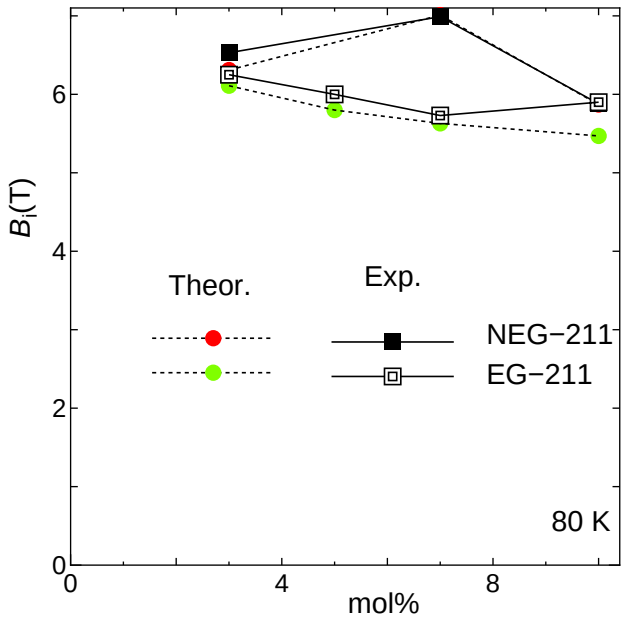

Fig. 4.12: Comparison of the irreversibility field B_i between experiment and theory.

Thus, it can be concluded that the dominant pinning centers which determine J_{cp} and B_i in NEG-123 superconductor are not the 211 particles but the nano-lamella structures. It

is speculated that the peak effect is caused by the order-disorder transition of flux lines with the assistance of the pinning by nano-lamella structures and that the deterioration of B_i with the volume fraction of the 211 phase is caused by the proximity effect of thin nano-lamella structures.

4. 4 Summary

In order to study the pinning mechanism of peak effect and irreversibility field in NEG-123 system, the variations in J_{cp} and B_i with volume fractions of EG-211 and NEG-211 phases were measured for $Nd_{0.33}Eu_{0.38}Gd_{0.28}Ba_2Cu_3O_y$ superconductor. It was found that J_{cp} increases but B_i decreases with increasing volume fraction both of EG-211 and NEG-211 phase and there was no large difference between these phases. This result shows a negative correlation between J_{cp} and B_i, suggesting that the mechanisms which determine J_{cp} and B_i are different. Based on the discussion on these results the following conclusions are obtained:

1. Since the peak effect became pronounced by addition of 211 phase, the change can be attributed to the 211 particles themselves or new defects nucleated by the addition. For the following reasons, it can be concluded that the 211 particles do not contribute for the peak effect: (a) the pinning force of 211 particles based on the pinning mechanisms of the condensation energy interaction decreases monotonically with increasing magnetic field and (b) since the size of 211 particles is much larger than the flux lines spacing, those can not contribute to the order-disorder transition of flux lines.
2. The pinning mechanism of the nano-lamella structures is the usual condensation energy interaction with the pinning strength which decreases monotonically with increasing field. Hence, these defects do not directly contribute to the peak effect. On the other hand, their size is sufficiently small that those can contribute to the peak effect with the aid of the order-disorder transition.
3. Since the irreversibility field is deteriorated by the addition of 211 phase, it can be concluded that the irreversibility field is not determined by the flux pinning of 211 particles. The decrease in B_i with the increasing fraction of 211 phase is considered to be caused by the proximity effect between thin superconducting region and high density of nano-lamellas.
4. The strong correlation between irreversibility field B_i and upper critical field B_{c2} also supports such speculation that the deterioration of B_i occurs due to the degradation of B_{c2} by the proximity effect.

References

1. D. Yoshimi, M. Migita, E. S. Otabe and T. Matsushita, *Physica C* **357-360**, 590, (2001)
2. T. Matsushita, D. Yoshimi, M. Migita and E. S. Otabe, *Supercond. Sci. Technol.* **14**, 732, (2001)
3. M. Muralidhar, M. R. Koblischka, T. Saitoh and M. Murakami, *Supercond. Sci. Technol.* **11**, 1349, (1998)
4. M. R. Koblischka, M. Muralidhar and M. Murakami, *Appl. Phys. Lett*. **73**, 2351, (1998)
5. A. K. Pradan, M. Muralidhar, M. R. Koblischka, M. Murakami, K. Nakao and N. Koshizuka, *Appl. Phys. Lett.* **75**, 253, (1999)
6. M. Muralidhar, M. R. Koblischka, P. Diko and M. Murakami, *Appl. Phys. Lett.* **76**, 91, (2000)
7. M. Muralidhar, K. Segawa and M. Murakami, *Materials Science and Engineering* B**65**, 42, (1999)
8. M. Muralidhar and M. Murakami, *Physica C* **363**, 19, (2001)
9. M. Muralidhar, N. Sakai, N. Chikumoto, M. Jirsa, T. Machi, M. Nishiyama, Y. Wu and M. Murakami, *Phys. Rev. Lett*. **89**, 237001-1, (2003)
10. M. Muralidhar, M. Jirsa, N. Sakai and M. Murakami, *Appl. Phys. Lett.* **79**, 3107, (2001)
11. M. Muralidhar, N. Sakai, M. Jirsa and M. Murakami, *IEEE. Trans. Appl. Superconductivity* **13**, 3091, (2003)
12. M. Muralidhar, N. Sakai, M. Jirsa and N. Koshizuka, *Appl. Phys. Lett*. **83**, 5005, (2003)
13. M. Muralidhar, N. Sakai, M. Jirsa, M. Murakami, N. Koshizuka and I. Hirabayashi, *Physica C* **426-431**, 196, (2005)
14. M. Murakami, S. Gotoh, H. Fujimoto, K. Yamaguchi, N. Koshizuka and S. Tanaka, *Supercond. Sci. Technol.* 4**,** S43 (1991)
15. M. Murakami, H. Fujimoto, S. Gotoh, K. Yamaguchi, N. Koshizuka and S. Tanaka, *Physica C* **185-189**, 321 (1991)
16. S. Awaji, N. Isono, K. Watanabe, M. Murakami, N. Koshizuka and K. Noto, *Phys. Rev. B* **69**, 214522-1, (2004).
17. T. Matsushita, *Supercond. Sci. Technol.* **13**, 730, (2000)

Chapter 5 Concluding remarks

This thesis describes the flux pinning mechanisms of peak effect and irreversibility field in newly developed $(Nd_{0.33}Eu_{0.38}Gd_{0.28})Ba_2Cu_3O_y$ bulk superconductors. Flux pinning properties were investigated with focusing on the origin of the high peak critical current density J_{cp} and irreversibility field B_i for this bulk superconductor with addition of NEG-211 and EG-211 secondary phase particles of the volume fractions up to 10 mol%. It was found that J_{cp} increases but B_i decreases with increasing volume fractions both of NEG-211 and EG-211 phases and there is no large difference between these phases. This results show a negative correlation between J_{cp} and B_i under a variation in the fraction of added 211 phase and suggests that the mechanisms which determine J_{cp} and B_i are different. Since the peak effect became pronounced by addition of 211 phase, the change can be attributed to the 211 particles themselves or to new defects nucleated by the addition of 211 phase. Based on the discussions the following conclusions are obtained:

(a) The 211 particles do not contribute to the peak effect neither directly through the pinning mechanisms of the condensation energy interaction nor indirectly with the aid of the order-disorder transition of flux lines.

(b) Another possible candidate for the peak effect is nano-lamella structure nucleated by addition of 211 phase. Although these defects do not directly contribute to the peak effect by the pinning mechanism of condensation energy interaction, those may contribute to it with the aid of the order-disorder transition of flux lines.

(c) On the other hand, the deterioration of B_i with increasing volume fraction of 211 phase particles can not be explained by the pinning of 211 particles themselves. The decrease in B_i is considered to be caused by the proximity effect of nano-lamella structures.

Recommended materials for various applications

According to the observed results of the critical current density and the irreversibility field, the following conclusion about recommended materials for practical application can be obtained:

Case-1: NEG -123 bulk superconductors with addition of 10 mol% NEG-211 which obtained highest J_c (about 6×10^8 A/m^2) at 2-5 T can be used for the purpose of motors, generators, magnetic separation device etc.

Case-2: NEG-123 bulk superconductors with addition of 3 mol% NEG-211 which

obtained highest irreversibility field (above 10 T) can be used for purpose of high field superconducting magnet.

Recommendations for further improvements of flux pinning

As the consequence, the following guides are obtained for the better performance of RE-123 bulk superconductors.

Case-1: To achieve further improvement of J_{cp}, it requires more investigation in NEG-123 system with addition above 10 mol% NEG-211 particles.

Case-2: To get more higher irreversibility field, it requires further investigation with addition below 3 mol% NEG-211 particles.

Appendix-1 The flux creep-flow model

1. 1 Flux creep phenomenon

When magnetic field is applied to a superconductor, magnetic field penetrates to the superconductor and flux lines are pinned by pinning center. At the same time, flux line tends to move by Lorentz force. These conditions are schematically shown in Fig. A1. The energy is periodically changed and decreasing according to increasing the position, x. The gradual decrease is representing the work done by the Lorentz force. In this figure, flux lines move in group unit and this group is called a flux bundle.

According to flux creep model, the possibility to jump over an energy barrier (activation energy), U, for one trial of flux bundle is given by $\exp(-U/k_{\mathrm{B}}T)$ which is known as Arrhenius expression. Here, k_{B} is Boltzmann constant and $k_{\mathrm{B}}T$ is thermal energy. If the flux bundle succeeded to jump over the activation energy, hopping distance is considered to be given by flux line spacing, a_f. According to the movement of the flux bundle, electric field is induced as

$$E = Ba_{\mathrm{f}}\nu_0\left[\exp\left(-\frac{U}{k_{\mathrm{B}}T}\right)-\exp\left(-\frac{U'}{k_{\mathrm{B}}T}\right)\right], \qquad (1)$$

where ν_0 is attempt frequency of the flux bundle, and U' is activation energy of opposite direction to Lorentz force.

Here, it will calculate a simple case of the relaxation of magnetization by the flux creep. A large slab superconductor $(0 \le x \le 2d)$ is placed in external magnetic field, H_{e} along z-axis. From the symmetry, it considered only the half region of $(0 \le x \le d)$. In the case of increasing magnetic field, induced current flows along y-axis and movement of the flux bundle by the flux creep is along x-axis. If the current density, J is assumed to be uniform, magnetic field flux density is given by $B = \mu_0(H_e - Jx)$. Therefore, observed electric field, E, at the surface of superconductor (x=0) is calculated from Maxwell equation, $rotE = -\partial B/\partial t$ is given by

$$E = \frac{\partial d\langle B\rangle}{\partial t} = -\frac{\mu_0 d^2}{2}\cdot\frac{\partial J}{\partial t}, \qquad (2)$$

where $\langle B\rangle$ is the average of magnetic flux density. If one have the relations, $U(J)$ and $U'(J)$ as function of J, relaxation of J as a function of

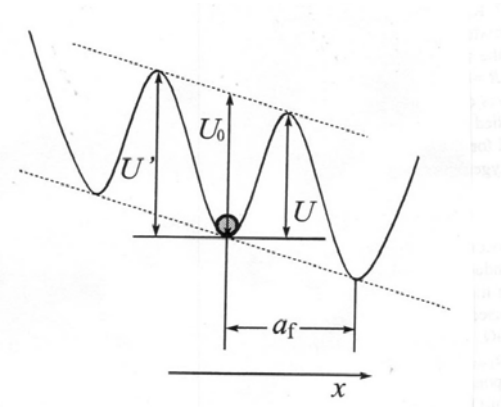

Fig. A1: Washboard pinning potential.

time is obtained by substituting Eq. (1) to Eq. (2).

When the relaxation is small, the effect of the flux creep is small. Then, it is supposed $U \ll U'$ and the second term of Eq. (1) can be neglected. Since, U decreases with increasing J, U can be expanded to

$$U = U_0^* - rJ. \qquad (3)$$

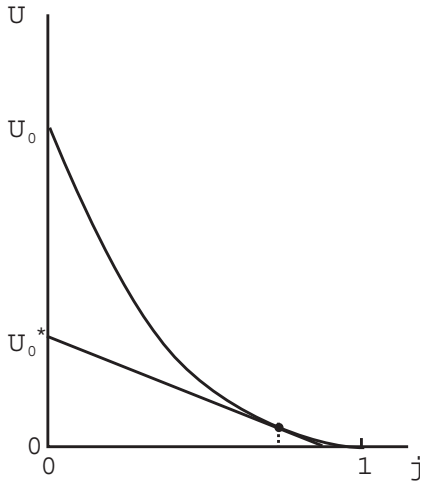

Fig. A2: Relation between activation energy, U, and normalized current density, $j = J / J_{c0}$.

Here U_0^* is the energy at $J \to 0$ and is called the apparent pinning potential as shown in Fig. A2. U_0^*, which is experimentally measured in relaxation rate of magnetization, is different from true pinning potential U_0. Because U_0 is only observed at $J \to 0$ and Eq. (3) is useful at $J \sim J_{c0}$, where J_{c0} is virtual critical current density obtained at $U = 0$. In other words, virtual critical current density is observed at the case of flux creep free. Therefore, it is approximately considered $r = U_0^* / J_{c0}$, and U is given by

$$U = U_0^* \left(1 - \frac{J}{J_{c0}} \right). \tag{4}$$

Hence from Eqs. (1), (2) and (4), we have

$$\frac{\partial J}{\partial t} = -\frac{2Ba_f \nu_0}{\mu_0 d^2} \exp\left[-\frac{U_0^*}{k_B T} \left(1 - \frac{J}{J_{c0}} \right) \right]. \tag{5}$$

This equation is easily solved under the condition $J = J_{c0}$ at $t = 0$ and we obtain

$$\frac{J}{J_{c0}} = 1 - \frac{k_B T}{U_0^*} \log\left(\frac{2Ba_f \nu_0 U_0^* t}{\mu_0 d^2 J_{c0} k_B T} + 1 \right). \tag{6}$$

Therefore, after a sufficient time, 1 in the argument of logarithm can be neglected. In this case, the logarithmic relaxation rate is given by

$$-\frac{d}{d \log t} \left(\frac{J}{J_{c0}} \right) = \frac{k_B T}{U_0^*}, \tag{7}$$

where U_0^* is obtained from experimental result. In usual case of experiment of relaxation of magnetization, initial magnetization, M_0, is used and in this case $J/J_{c0} \to M/M_0$ for Eq. (7).

According to the result investigated by Welch[1], the relation between apparent pinning potential and true pinning potential is given for sinusoidal pinning potential well as

$$U_0^* = 1.65 (k_B T U_0^2)^{1/3}. \tag{8}$$

Therefore, true pinning potential can be estimated from apparent pinning potential observed from relaxation of magnetization.

1. 2 Flux creep in sinusoidal washboard potential

Here it estimates current density dependence of activation energy, $U(j)$, for sinusoidal washboard potential as shown in Fig. A2, where j is normalized current density given by $j = J/J_{c0}$. The washboard potential is assumed by

$$F(x) = \frac{U_0}{2}\sin kx - fx \tag{9}$$

as shown in Fig. A1. In the above $k = 2\pi / a_f$ and $f = JBV$ is Lorentz force to the flux bundle, where V is volume of flux bundle. The local equilibrium position of the flux bundle is obtained by differentiating of Eq. (9) and given by

$$x = -x_0 = -\frac{1}{k}\cos^{-1}\left(\frac{2f}{U_0 k}\right). \tag{10}$$

On the other hand, F(x) is maximum at $x = x_0$. Therefore activation energy is obtained by $U = F(x_0) - F(-x_0)$ and is

$$\frac{U}{U_0} = \left[1 - \left(\frac{2f}{U_0 k}\right)^2\right]^{1/2} - \left(\frac{2f}{U_0 k}\right)\cos^{-1}\left(\frac{2f}{U_0 k}\right). \tag{11}$$

If there is no thermal agitation, virtual critical state is achieved and $U = 0$ is obtained. In this case, x_0 is equal to 0 and $2f / U_0 k = 1$ is satisfied. Therefore, J is equal to virtual critical current density in the case of flux creep free, J_{c0}. Hence, the following relation is obtained,

$$\left(\frac{2f}{U_0 k}\right) = \frac{J}{J_{c0}} \equiv j. \tag{12}$$

From this equation, Eq. (11) is written as

$$U(j) = U_0\left[(1 - j^2)^{1/2} - j\cos^{-1} j\right]. \tag{13}$$

From the relationship,

$$U' \approx U + \pi U_0 \frac{J}{J_{c0}}, \tag{14}$$

Eq. (1) can written by

$$E = Ba_f \nu_0 \exp\left[-\frac{U(j)}{k_B T}\right]\left[1 - \exp\left(-\frac{\pi U_0 j}{k_B T}\right)\right]. \tag{15}$$

Therefore, *E-J* characteristics can be calculated under the assumption of U_0 and J_{c0}. Attempt frequency of the flux bundle, ν_0, for flux creep is investigated[2] and given by

$$\nu_0 = \frac{\zeta \rho_f J_{c0}}{2\pi a_f B}, \tag{16}$$

where ζ is a conatant dependent on the kind of pinning center and $\zeta \cong 2\pi$ is obtained for the case of point like pinning center[3], $\zeta = 4$ is obtained for the case of large normal pinning center[4]. ρ_f is related with normal resistivity and according to Bardeen-Stephen model[5], ρ_f is related with normal resistivity ρ_n and given by

$$\rho_f = \frac{B}{B_{c2}} \rho_n . \tag{17}$$

ρ_n is approximately given by

$$\rho_n(T) = \frac{T}{T_c} \rho_n(T_c). \tag{18}$$

1. 3 TAFF (Thermally Activated Flux Flow)

If the second term of Eq. (14) is smaller than $k_B T$, Eq. (1) is written as

$$E \cong \frac{\pi B a_f \nu_0 U_0 J}{J_{c0} k_B T} \exp\left(-\frac{U_0}{k_B T} \right), \tag{19}$$

and is linear *E-J* characteristics. This condition is known as TAFF (Thermally Activated Flux Flow). After enough relaxation at high temperature or high magnetic field, TAFF can be observed. Here if *J* is sufficiently small, $U \rightarrow U_0$ is achieved and resistivity is given by

$$\rho = \rho_0 \exp\left(-\frac{U_0}{k_B T} \right), \tag{20}$$

where ρ_0 is equal to $\pi B a_f \nu_0 U_0 / J_{c0} k_B T$. From above result, it is found that the resistivity under flux creep does not reach zero due to finite electric field at finite temperature. On the contrary, there are many discussions [6,7] that if resisitivity will be zero at $J \rightarrow 0$ which represents real superconducting state ($R = 0$) at finite temperature based on theory of glass-liquid transition of flux lines.

1. 4 Pinning potential

In this subsection, it assumed pinning potential, U_0, which is most important parameter in the phenomenon of the flux creep.

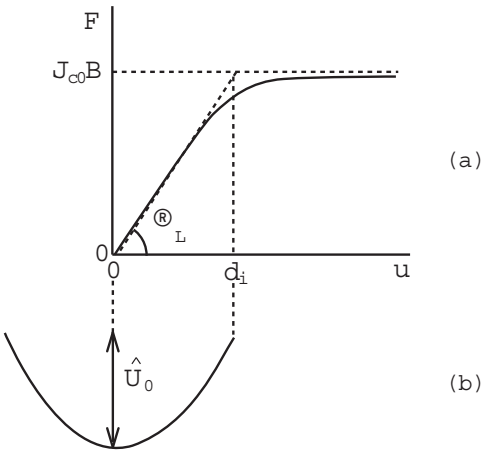

Fig. A3: (a) average pinning force density vs. displacement of flux lines. (b) pinning potential for unit volume of flux line, $\hat{U}_0$

Figure A3 shows the relationship between pinning force density and displacement of flux line. $\hat{U}_0$ represent pinning potential for unit volume of flux line. When the displacement u is small enough, pinning force density increases linearly, and phenomenon is reversible in this region. On the other hand, it changes to nonlinear and irreversible characteristics, and pinning force density is finally saturated to $J_{c0}B$, when u reaches to interaction distance, d_i. Therefore, $\hat{U}_0$ can be estimated from the present pinning force density-displacement characteristic of reversible region. Here $\hat{U}_0$ is given by

$$\hat{U}_0 = \frac{\alpha_L d_i^2}{2}, \qquad (21)$$

where α_L is Labusch parameter. Virtual critical current density J_{co} of flux creep free case is related with α_L and d_i as

$$J_{c0}B = \alpha_L d_i. \qquad (22)$$

On the other hand, d_i is given by[8]

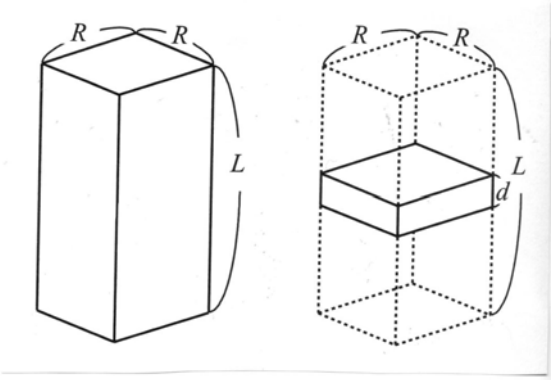

(a) (b)

Fig. A4: Volume of flux bundle, V. (a) When longitudinal flux bundle size, L, is smaller than thickness of superconductor, d, $V = LR^2$. (b) When L is larger than d, $V = dR^2$.

$$d_{\mathrm{i}} = \frac{a_{\mathrm{f}}}{\zeta}, \tag{23}$$

where ζ is a constant depended on the kind of pinning center as abovementioned. Then we have pinning potential U_0 of flux bundle as

$$U_0 = \hat{U}_0 V, \tag{24}$$

where V is the volume of flux bundle. V is estimated from the size of flux bundle in longitudinal direction, L and transverse direction R given by

$$L = \left(\frac{C_{44}}{\alpha_{\mathrm{L}}} \right)^{1/2}, \tag{25}$$

$$R = \left(\frac{C_{66}}{\alpha_{\mathrm{L}}} \right)^{1/2}, \tag{26}$$

as shown in Fig. A4. In the above, C_{44} is the tilt modulus of flux lines and given by

$$C_{44} = \frac{B^2}{\mu_0}. \tag{27}$$

On the other hand, C_{66} is shear modulus of flux lines and is largely dependent on the condition of flux line lattice. In the case of perfect triangular lattice in three dimensional, C_{66} takes maximum value of

C_{66}^0, and it is given by[9]

$$C_{66}^0 = \frac{B_c^2 B}{4\mu_0 B_{c2}}\left(1-\frac{B}{B_{c2}}\right)^2, \tag{28}$$

and decreases with disorder of flux line lattice, then reaches to zero when flux line lattice is in melt condition.

1. 5 Number of flux lines in the flux bundle, g^2

It is considered that transverse flux bundle size, R is the order of a_f of several times larger except the case of very weak pinning of superconductor. In the case of very strong pinning force, R is smaller than a_f. Although, the size is not smaller than flux line spacing, R is expresses as

$$R = ga_f, \tag{29}$$

where $g^2(\geq 1)$ is the number of flux lines in the flux bundle. Therefore, g^2 is given by Eqs. (26) and (29)

$$g^2 = \frac{C_{66}}{\zeta J_{c0} B a_f}. \tag{30}$$

For the case of three dimensional perfect triangle flux line lattice, g^2 takes maximum value, g_e^2, and it is given by[10]

$$g_e^2 = \frac{C_{66}^0}{\zeta J_{c0} B a_f}. \tag{31}$$

As abovementioned, the value of C_{66} is largely dependent on the condition of flux line lattice and changes from maximum value of C_{66}^0 to zero, and there is no straightforward method to determine the flux bundle size. Therefore, it is assumed based on minimization of energy dissipation that g^2 is determined so as to achieve maximum critical current density under flux creep [10]. According to the theory, g^2 is given as

$$g^2 = g_e^2\left[\frac{5k_B T}{2U_e}\log\left(\frac{Ba_f\nu_0}{E_c}\right)\right]^{4/3}, \tag{32}$$

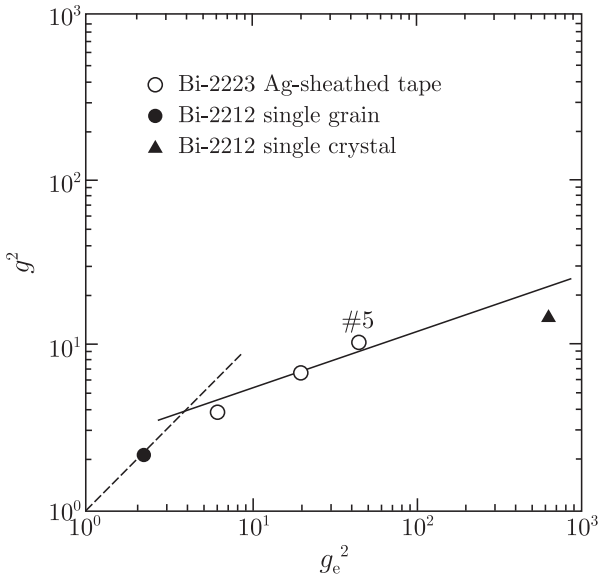

Fig. A5: g^2 is obtained from experimental result and g_e^2 predicted by elastic theory[10].

Solid line represents the relation of Eq. (33).
where U_e is the pinning potential at $g = g_e$ and E_c is criteria of electric field, respectively. From the relationship of $U_e \propto g_e$, we have

$$g^2 \propto g_e^{2/3}. \tag{33}$$

In Fig. A5, the relationship between g^2 and g_e^2 is shown. g^2 is from the result of irreversibility field as aforementioned and is quantitatively explained from Eq. (33).
When the size of a bulk superconductor is larger than L and R, the volume of flux bundle is given by

$$V = LR^2, \tag{34}$$

and the pinning potential is given by

$$U_0 = \frac{0.835 g^2 k_B J_{c0}^{1/2}}{\zeta^{3/2} B^{1/4}}. \tag{35}$$

on the other hand, if thickness of superconductor d is smaller than L such as a thin film, V is given by

$$V = dR^2, \tag{36}$$

and U_0 is given by

$$U_0 = \frac{4.23 g^2 k_B J_{c0} d}{\zeta B^{1/2}}. \tag{37}$$

1. 6 Irreversibility field

Before explanation of numerical calculation by the flux creep theory, it is explained that irreversibility is analytically given by U_0 derived above. First it was assumed that the second term in Eq. (15) is neglected. Irreversibility field is given by the field at J_c = 0 with defined by the electric field criteria $E = E_c$. Therefore from Eq. (15) we have,

$$E_c = Ba_f \nu_0 \exp\left(-\frac{U_0}{k_B T}\right). \tag{38}$$

If it assumed that the temperature and magnetic field dependences of J_{c0} as

$$J_{c0} = A\left[1-\left(\frac{T}{T_c}\right)^2\right]^m B^{\gamma-1}\left(1-\frac{B}{B_{c2}}\right)^\delta, \tag{39}$$

where A, m, γ and δ are pinning parameters. Eq. (39) is usually used in conventional metal superconductor and known as scaling law of the critical current density. For the case $d > L$ of larger bulk superconductor, irreversibility field B_i is given by

$$B_i^{(3-2\gamma)/2} = \left(\frac{K_1}{T}\right)^2\left[1-\left(\frac{T}{T_c}\right)^2\right]^m\left(1-\frac{B_i}{B_{c2}}\right)^\delta. \tag{40}$$

In the above, K_1 is a constant depended on pinning force density as

$$K_1 = \frac{0.835 g^2 A^{1/2}}{\zeta^{3/2}\log(B_i a_f \nu_0 / E_c)}. \tag{41}$$

On the other hand, for the case $d < L$ such as thin film superconductor, B_i is given by

$$B_i^{(3-2\gamma)/2} = \frac{K_2}{T}\left[1-\left(\frac{T}{T_c}\right)^2\right]^m\left(1-\frac{B_i}{B_{c2}}\right)^\delta d, \tag{42}$$

where K_2 is given by

$$K_2 = \frac{4.23 g^2 A}{\zeta\log(B_i a_f \nu_0 / E_c)}. \tag{43}$$

In practical case, $\log(B_i a_f \nu_0 / E_c)$ can safely be regarded as a constant from 14 to 20, since it is very weakly depended on B_i.

If temperature is near critical temperature, T_c, B_i is far below upper critical field, H_{c2} and $(1\text{-}B_i/B_{c2})^\delta$ in right hand side of Eq. (40) can be regarded as unity. In addition $(K_1 / T)^2$ can be approximately put as a constant $(K_1 / T_c)^2$.

$$B_{\mathrm{i}} \propto \left[1-\left(\frac{T}{T_{\mathrm{c}}}\right)^{2}\right]^{ni}, \qquad (44)$$

where temperature index of irreversibility field, n_i is given by

$$n_{\mathrm{i}} = \frac{2m}{3-2\gamma}. \qquad (45)$$

For example, in the case of Y-123, it is known that the parameters are given as m = 3/2 and γ = 1/2, since the dominant pinning center at high temperature is known as Y-211 precipitates. Then we have n_i = 3/2 and the temperature dependence of B_{i} is predicted as $B_{\mathrm{i}} \propto \left[1-(T/T_{\mathrm{c}})^{2}\right]^{3/2}$. This result is well known as reported by Yeshurun and Malozemoff at very early stage [11].

1. 7 Flux creep-flow model

For calculation of E-J characteristics, current density is not always smaller than J_{c0}, electric field E_{ff} is induced by flux flow, and is given by

$$\begin{aligned} E_{\mathrm{ff}} &= 0; && j \le 1 \\ &= \rho_{\mathrm{f}}(J - J_{\mathrm{c0}}); && \mathrm{j}>1 \end{aligned} \qquad (46)$$

where ρ_{f} is given by Eq. (17). On the other hand, electric field by flux creep, E_{cr}, is considered to remain and assumed as [12, 13]

$$E_{\mathrm{cr}} = Ba_{\mathrm{f}}\nu_0 \exp\left[-\frac{U(j)}{k_{\mathrm{B}}T}\right]\left[1-\exp(-\frac{\pi U_0 j}{k_{\mathrm{B}}T})\right]; \qquad j \le 1,$$

$$= Ba_{\mathrm{f}}\nu_0\left[1-\exp(-\frac{\pi U_0}{k_{\mathrm{B}}T})\right]; \qquad j > 1, \qquad (47)$$

Then, the total electric field, E, is obtained from E_{cr} and E_{ff} and is approximately given by

$$E = (E_{\mathrm{cr}} + E_{\mathrm{ff}})^{1/2}. \qquad (48)$$

In the above, E is approached to E_{cr} at j<1 and to E_{ff} at j>>1.

In usual oxide superconductor, pinning force density is known to be largely distributed. Here only parameter A in Eq. (39) is assumed to have the following distribution:

$$f(A) = K \exp\left[-\frac{(\log A - \log A_{\mathrm{m}})^2}{2\sigma^2} \right], \tag{49}$$

where A_{m} is the most probable value, K is a constant determined by the condition of normalization and σ^2 is a constant representing the degree of distribution width of pinning force density. Therefore, total electric field is given by

$$E(J) = \int_0^\infty Ef(A)dA. \tag{50}$$

References

1. D.O. Welch, *IEEE Trans. Magn.,* **27**, 1133 (1964)
2. K. Yamafuji, T. Fujiyoshi, K. Toko, T. Matsushita, *Physica C*, **159**, 743 (1989)
3. A.M. Campbell, H. Kupfer, R. Meier-Hirmer, *Proc. Int. Symp. On Flux Pinning and Electromagnetic Properties in Superconductors,* Fukuoka, 54 (1985)
4. T. Matsushita, *Jpn. J. Appl. Phys.*, **20**, 1995 (1981)
5. J. Bardeen, M. J. Stephen, *Phys. Rev.,* **140**, A1197 (1965)
6. D. S. Fisher, M. P. A. Fisher, D. A. Huse, *Phys. Rev.,* B**43**, 130 (1991)
7. M. P. A. Fisher, *Phys. Rev. Lett*., **62**, 1415 (1989)
8. E. H. Brandt, *Phys. Rev.*, B**34**, 6514 (1986)
9. T. Matsushita, T. Fujiyoshi, K. Toko, K. Yamafuji, *Appl. Phys. Lett.*, **56**, 2039 (1990)
10. T. Matsushita, *Physica C,* **217**, 461 (1993)
11. Y. Yeshurun, A. P. Malozemo, *Phys. Rev. Lett.*, **60**, 2202 (1988)
12. T. Matsushita, N. Ihara, *Proc. 7th Int. Workshop on Critical Currents in Superconductors,* **169,** World Scientific, Singapore (1994)
13. T. Matsushita, T. Tohdoh, N. Ihara, *Physica C*, **259**, 321 (1996)